

How accurate are foundational machine learning interatomic potentials for heterogeneous catalysis?

Luuk H. E. Kempen^{1,*}, Raffaele Cheula¹, and Mie Andersen^{1,*}

¹Center for Interstellar Catalysis, Department of Physics and Astronomy, Aarhus University, Aarhus C, Denmark

*Corresponding authors: luuk@phys.au.dk, mie@phys.au.dk

December 19, 2025

Foundational machine learning interatomic potentials (MLIPs) are being developed at a rapid pace, promising closer and closer approximation to *ab initio* accuracy. This unlocks the possibility to simulate much larger length and time scales. However, benchmarks for these MLIPs are usually limited to ordered, crystalline and bulk materials. Hence, reported performance does not necessarily accurately reflect MLIP performance in real applications such as heterogeneous catalysis. Here, we systematically analyze zero-shot performance of 80 different MLIPs, evaluating tasks typical for heterogeneous catalysis across a range of different data sets, including adsorption and reaction on surfaces of alloyed metals, oxides, and metal-oxide interfacial systems. We demonstrate that current-generation foundational MLIPs can already perform at high accuracy for applications such as predicting vacancy formation energies of perovskite oxides or zero-point energies of supported nanoclusters. However, limitations also exist. We find that many MLIPs catastrophically fail when applied to magnetic materials, and structure relaxation in the MLIP generally increases the energy prediction error compared to single-point evaluation of a previously optimized structure. Comparing low-cost task-specific models to foundational MLIPs, we highlight some core differences between these model approaches and show that—if considering only accuracy—these models can compete with the current generation of best-performing MLIPs. Furthermore, we show that no single MLIP universally performs best, requiring users to investigate MLIP suitability for their desired application.

1 Introduction

Data-driven molecular and materials modelling has seen enormous progress in the last five years [1–3]. This development has been driven by advances in graph neural networks and other novel architectures [4–19] as well as the assembly of large data sets with millions of calculated materials or molecules [20–29]. Together, these have enabled foundational machine learning interatomic potentials (MLIPs)—also known as pretrained or universal MLIPs—that can be applied at a very low computational cost across the periodic table *with reasonable, but varying, accuracy* [30–35].

Despite these advances, MLIPs are typically benchmarked on test splits of the same data sets they were trained on. Such benchmarks rarely reflect their performance in real applications such as heterogeneous catalysis. For instance, real catalysts may be amorphous (i.e., they lack long-range order) and may dynamically adapt their shape and composition according to the reaction conditions [36, 37]. In contrast, benchmark data sets usually contain ordered, crystalline materials. The Matbench Discovery framework, for instance, focuses on evaluating crystal stability predictions [38]. A further limitation is that MLIPs are often trained to reproduce stable structures and energies. For heterogeneous catalysis, however, we also require accurate pre-

dictions of reaction barriers, i.e., both adsorption and transition state (TS) energies [39–41]. These are then incorporated into microkinetic models to determine reaction mechanisms, catalyst activity, and product selectivity [42, 43]. Because rates depend exponentially on barriers, a very high accuracy is required both from the MLIP and from the underlying method used to generate the training data, typically density functional theory (DFT).

In this work we critically assess the performance of a wide range of recently developed foundational MLIPs for typical tasks in heterogeneous catalysis modelling (Figure 1), including the calculation of surface vacancy formation energies, adsorption energies, TS energies, and vibrational properties in the form of zero-point vibrational energies. We show that both the MLIP architecture as well as the data set it has been trained on are important factors in determining MLIP performance. Generally, the eSEN, Orb, and UMA models are among the best-performing models across most of the evaluated properties, and no single model stands out as being best across all data sets and properties evaluated in this work. This highlights the need for exploring MLIP performance for a desired application before choosing a model. We further highlight that a large number of evaluated MLIPs catastrophically fail when applied to surfaces containing magnetic materials. We

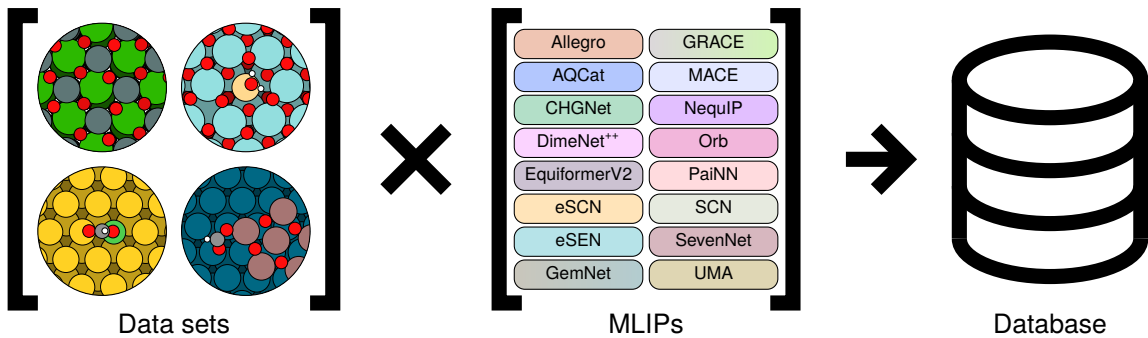


Figure 1: An overview of the data sets and foundational MLIPs assessed in this work.

identify a clear correlation between this catastrophic failure and the training data sets utilized to train the various MLIPs. While most of the comparisons in this work are done using DFT-relaxed geometries as reference to enable screening of a large number of models, we also analyze the effect of MLIP relaxation on a smaller subset of data, showing that this increases the error of the best-performing models. Finally, we compare the performance of MLIPs to that of low-cost, task-specific models trained on the analyzed data sets, highlighting areas where current-generation foundational potentials are lagging behind these task-specific models when used out-of-the-box (zero-shot), without fine-tuning.

2 Methods

2.1 Data collection

For this study, a database (Figure 1) was built up containing potential energy evaluations of 6 data sets with relevance to catalysis (see Section 2.2), using 80 different pretrained foundational MLIPs (see Section 2.3). The creation of this database was largely automated by a workflow that evaluates and stores results after specifying a combination of data set, MLIP, and result type (for example, potential energy) to obtain. These results are stored in a database, after which analysis can be performed by calculating target properties (such as reaction energy) from the relevant results (in case of reaction energy, the potential energies of pairs of initial and final states). This high-throughput screening is enabled by using the atomic simulation environment (ASE) [44] interfaces exposed by the various MLIP packages.

To enable the possibility of screening this large amount of models, the primary focus of this work is on single-point energy evaluations of DFT-relaxed geometries. This is not a fully realistic use case, though, as a DFT relaxation is computationally expensive and would practically be replaced by MLIP relaxations. At this scale, however, that also becomes computationally expensive. Hence, we discuss this more realistic use case only for a smaller subset of the data sets (Section 3.4).

2.2 Data sets

The data sets utilized in this study can broadly be divided into three categories: perovskite oxide sur-

faces, reactions on alloyed metal and oxide surfaces, and metal–oxide interfaces. These data sets are summarized in Table 1.

2.2.1 Perovskite oxide surfaces

The perovskite oxide surface data set, obtained from Taylor *et al.* [45], explores the energetics of nine (001) perovskite oxide (ABO_3) surfaces ($A = \text{Ca, Sr, Ba}$; $B = \text{Ti, Zr, Sn}$). This data set includes AO and BO_2 surface terminations of all perovskite oxides, as well as vacancies of A , B and O sites at various depths in the slabs. The target DFT energies in this data set were evaluated using the Vienna *ab initio* simulation package (VASP) [46, 47], using the projector augmented-wave (PAW) method [48] and a plane-wave basis set energy cutoff of 700 eV. The exchange–correlation functional was approximated using the Perdew–Burke–Ernzerhof (PBE) functional [49]. More details on the creation of this data set can be found in Taylor *et al.* [45].

The target property evaluated for this data set in this study is the slab vacancy formation energy, which is defined by Taylor *et al.* [45] with respect to the corresponding bulk vacancy as

$$E_{\text{form},X}^i = (E_{X\text{-vac}}^i + N_{\text{cells}}E_{ABO_3}^{\text{bulk}}) - (E_{\text{slab}}^i + E_{X\text{-vac}}^{\text{bulk}}), \quad (1)$$

where $E_{X\text{-vac}}^i$ is the energy of the slab with site X vacated and surface termination i , $E_{ABO_3}^{\text{bulk}}$ is the energy of the bulk perovskite oxide, E_{slab}^i is the energy of the pristine slab with surface termination i , and $E_{X\text{-vac}}^{\text{bulk}}$ is the energy of the bulk perovskite oxide with site X vacated. N_{cells} describes how many supercells of the bulk perovskite oxide are included in the vacated bulk perovskite oxide system, which is 8 ($2 \times 2 \times 2$) for this data set.

2.2.2 Reactions on alloyed metal and oxide surfaces

The category of reactions on alloyed metal and oxide surfaces encompasses two data sets. The first data set, obtained from Cheula *et al.* [50], concerns the $\text{ZrO}_2(101)$ surface, both pristine and doped with 16 different metals. The target DFT energies in this data set were evaluated using Quantum Espresso [51, 52] with

the PBE exchange–correlation functional [49] and pseudopotentials from the SSSP library [53]. A plane-wave basis set was used with a plane-wave cutoff energy of 40 Ry (~ 544 eV) and an electronic density cutoff energy of 320 Ry (~ 4354 eV). A Hubbard U correction of 4 eV was applied to the d orbitals of Zr atoms [54, 55]. Elementary reaction steps for CO₂ hydrogenation to methanol were investigated on the pristine ZrO₂ surface as well as 8 metal-doped surfaces. More details on the creation of this data set can be found in Cheula *et al.* [50].

Four target properties are evaluated for the data set in this study. The first two are the activation energy E_{act} and reaction energy ΔE_{r} for elementary reaction steps. The final two are the formation energies for adsorbates and TSs with respect to the clean slabs and gas-phase H₂, H₂O, and CO₂ following the definition by Cheula *et al.* [50]:

$$E_{\text{form}} = E_{\text{slab+ads}} - E_{\text{slab}} - N_{\text{C}}E_{\text{C}} - N_{\text{O}}E_{\text{O}} - N_{\text{H}}E_{\text{H}}, \quad (2)$$

where $E_{\text{slab+ads}}$ is the energy of a slab with adsorbate or TS, E_{slab} is the energy of a clean slab, N_i are the number of atoms of species i in the adsorbate, and E_i are reference energies of these atoms. These reference energies are calculated with H₂, H₂O, and CO₂ as reference, such that

$$E_{\text{H}} = \frac{1}{2}E_{\text{H}_2}; \quad (3)$$

$$E_{\text{O}} = E_{\text{H}_2\text{O}} - E_{\text{H}_2}; \quad (4)$$

$$E_{\text{C}} = E_{\text{CO}_2} - 2E_{\text{O}}. \quad (5)$$

The second data set, obtained from Cheula & Andersen [56], encompasses (111) and (100) facets of 6 pure metals and 12 single-atom alloys (SAAs), including elementary reaction steps for the reverse water–gas shift (RWGS) reaction. The target DFT energies in this data set were evaluated using the same DFT settings as in the (doped) ZrO₂(101) data set outlined above, with the exception of using the BEEF-vdW exchange–correlation functional [57] instead of PBE and without Hubbard U correction. The same target properties were evaluated as for the (doped) ZrO₂(101) data set: activation energy, reaction energy, and adsorbate and TS formation energy. However, in this case, analogous to the earlier work, the formation energies are defined with respect to gas-phase H₂, H₂O, and CO, such that in this case

$$E_{\text{C}} = E_{\text{CO}} - E_{\text{O}} \quad (6)$$

is substituted into Equation (2).

2.2.3 Metal–oxide interfaces

The category of metal–oxide interfaces encompasses three closely-related data sets.

The first data set, obtained from Kempen & Andersen [58], includes global minima of metal oxide (Zn _{y} O _{x} and In _{y} O _{x}) nanoclusters on metal (Cu, Pd, and Au) surfaces. The target DFT energies in this data set were evaluated using the GPAW package [59–61],

which implements the PAW method [48], with the PBE exchange–correlation functional [49]. The wave functions were represented using a plane-wave basis with a plane-wave energy cutoff of 400 eV for Cu- and Au-supported systems, and 500 eV for Pd-supported systems. A $2 \times 2 \times 1$ Monkhorst–Pack k -point grid [62] was utilized for Brillouin zone sampling. More details on the creation of this data set can be found in Kempen & Andersen [58].

The target property evaluated for this data set is the zero-point energy of the nanoclusters, used by Kempen & Andersen [58] to perform a free energy analysis. The zero-point energy is evaluated in the harmonic limit, considering only the vibrational modes of the nanocluster atoms. To evaluate vibrational modes, the nanoclusters were relaxed to a force criterion of $F_{\text{max}} = 0.01$ eV Å⁻¹ after which the cluster atoms were individually displaced in the positive and negative direction of the three Cartesian coordinate axes with a step size of 0.01 Å to calculate a second-order central finite difference approximation of the Hessian matrix, as implemented in the ASE vibrations module [44]. The zero-point energy is then given as

$$E_{\text{ZPE}} = \frac{1}{2} \sum_{i=1}^{3N} \varepsilon_i, \quad (7)$$

where ε_i is the vibrational energy of mode i .

The second data set, obtained from Nielsen *et al.* [63], includes a large range of formate (HCOO) adsorbates on the metal-supported metal oxide nanoclusters described above, including both global minima and local minima of the nanoclusters within 0.1 eV of the global minimum energy structure. The target DFT energies in this data set were evaluated with the GPAW package [59–61] and the PBE exchange–correlation functional [49] with D4 dispersion corrections [64–66]. A plane-wave energy cutoff of 400 eV was used for all systems, as well as a $2 \times 2 \times 1$ Monkhorst–Pack k -point grid [62]. More details on the creation of this data set can be found in Nielsen *et al.* [63].

The target property evaluated for the data set in this study is the adsorption energy of the formate adsorbate, defined as

$$E_{\text{ads}} = E_{\text{cluster+ads}} - E_{\text{cluster}} - E_{\text{HCOO (g)}}, \quad (8)$$

where $E_{\text{cluster+ads}}$ is the energy of a nanocluster with the adsorbate, E_{cluster} is the energy of the clean nanocluster, and $E_{\text{HCOO (g)}}$ is the energy of gas-phase formate.

The third data set, obtained from Kempen *et al.* [67], includes initial, final, and TSs for the CO₂ + H \rightleftharpoons HCOO elementary reaction step on In _{y} O _{x} /Cu(111) inverse catalyst systems. The target DFT energies in this data set were evaluated using the GPAW package [59–61] and the PBE exchange–correlation functional [49] with D4 dispersion corrections [64–66]. A plane-wave energy cutoff of 600 eV was used for all systems, as well as a $2 \times 2 \times 1$ Monkhorst–Pack k -point grid [62]. More details on the creation of this data set can be found in Kempen *et al.* [67].

The target properties evaluated for this data set in this study are the activation energy E_{act} and reaction energy ΔE_r for the $\text{CO}_2 + \text{H} \rightleftharpoons \text{HCOO}$ reaction step on the different active sites.

2.3 Machine learning interatomic potentials

In this study, 80 different pretrained MLIPs have been utilized, spanning 16 different families—groups of models with broadly the same architecture. A short description of each of these families, and the pretrained models within each architecture, is given below. We further specify which training data sets the pretrained models have been trained on. Here, we denote combination of data sets A and B as ‘A + B,’ and pre-training on data set A followed by fine-tuning on data set B as ‘A → B.’ A full overview of all models included in this study is given in Table S1.

CHGNet [30] is a GNN architecture where magnetic moments are explicitly included. We evaluated CHGNet performance with the model trained on the MPTrj data set [30].

DimeNet⁺⁺ [5] is a GNN architecture where messages between atoms are embedded in addition to atomic features. We evaluated DimeNet⁺⁺ performance with the model trained on OC20-All [20].

GemNet [6] is based on DimeNet⁺⁺, but utilizes geometric message passing and is equivariant. We evaluated GemNet-dT performance with the models trained on OC20-All [20], as well as OC22 [21]. GemNet-OC [7] is a further development of GemNet, specifically built for the OC20 data set. We evaluated GemNet-OC performance with the models trained on OC20-All [20] as well as on OC22, OC20-All + OC22, and OC20 → OC22 [21].

The PaiNN architecture [4] is another example of an equivariant GNN. Here, we evaluated PaiNN performance with the model trained on OC20-All [20].

The NequIP network architecture [8, 9] is an equivariant GNN architecture. NequIP MLIPs with $\ell_{\text{max}} = 3$ (maximum spherical harmonic rotation order included in the basis set) and 6 message-passing layers are available, trained on both MPTrj [30] and OMat24 → MPTrj + sAlex (OAM) [22].

Similarly, the Allegro network architecture [9, 10] is an equivariant graph neural network architecture. Allegro MLIPs with $\ell_{\text{max}} = 3$ and 4 message-passing layers are available, trained on both MPTrj [30] and OAM [22].

SevenNet [11] is based on the NequIP architecture, introducing a parallelization scheme for scaling to larger systems via spatial decomposition. While this feature is not relevant for the application in this study, we still evaluated the four currently available pretrained SevenNet models. These include two models trained on MPTrj [30] (one larger model with $\ell_{\text{max}} = 3$), one model trained on OMat24 [22], and one model trained simultaneously on MPTrj, OMat24, and sAlex [22] using multi-fidelity learning [32]. Performance of this latter model was evaluated for both MPTrj + sAlex and

OMat24 tasks.

The MACE architecture [12] combines equivariant message passing with atomic cluster expansion (ACE). The MACE foundation models [31] pretrained on MPTrj [30] (MP-0a in three sizes and MP-0b3), MPTrj + sAlex [22, 30], OMat24 [22], and MatPES-PBE [23] were used to evaluate MACE model performance.

Similarly, the GRACE architecture [13] is an extension of ACE, incorporating graphs. GRACE foundation models [33] with one- and two-layer architectures, three sizes, and trained on MPTrj [30], OMat24 [22], and OAM [22] have been used to evaluate GRACE model performance.

The Orb family of models [34] is trained using diffusion pretraining with subsequent fine-tuning. Their architecture is not equivariant by default, but equivariance is approximated using equigrad, a regularization scheme. All eight publicly-released Orb models—combinations of the three key variables conservatism (direct or conservative), maximum neighbor limits (20 or infinity), and training data set (MPTrj + Alex [24, 30] or OMat24 [22])—were used to evaluate Orb model performance.

The SCN architecture [14] is a GNN architecture utilizing spherical functions. We evaluated SCN performance with the models trained on OC20-2M and OC20-All+MD [20].

The eSCN architecture [15] builds on SCN by enforcing equivariance in message passing. We evaluated eSCN performance with the two models trained on OC20-All+MD [20]: one with $M = 2$ and 12 layers, and one with $M = 3$ and 20 layers.

The EquiformerV2 architecture [17] builds on Equiformer [16], an equivariant GNN, by introducing eSCN convolutions, among other tweaks. We evaluated EquiformerV2 performance with the 31M, 86M (83M for OC20), and 153M models trained on MPTrj [30], OMat24 [22], OAM [22], and OC20 (OC20-All+MD for 31M and 153M, and OC20-2M for 83M) [20]. We additionally evaluated performance with the DeNS models [18] trained on MPTrj, which introduce an auxiliary task to denoise non-equilibrium structures, and with the publicly-available model trained on OC22 ($\lambda_E = 4$, $\lambda_F = 100$), which has 121M parameters [21].

The eSEN architecture [19] builds on eSCN and Equiformer, with a number of changes to the internal architecture of the convolution blocks to obtain smooth models. We evaluated eSEN performance with the 30M models [19] trained on MPTrj [30], OMat24 [22], and OAM [22], as well as with the publicly available small and medium models trained on OC25 (eSEN-S-cons. and eSEN-M-d.) [25].

The UMA architecture [35] builds on eSEN, expanding its input to incorporate a global embedding based on total charge, spin multiplicity, and the DFT task. Incorporation of the DFT task allows the model to be trained on a mix of DFT tasks. Furthermore, UMA introduces a mixture of linear experts to increase the model size while keeping inference times manageable. UMA models have been trained on a combination of

Table 1: Overview of the data sets utilized in this study.

Data set	Ref.	Target properties (number of entries)
Perovskite oxide surfaces	[45]	Slab vacancy formation energy (305)
Reactions on (doped) zirconia	[50]	Activation energy (62) Reaction energy (62) Adsorbate formation energy (122) TS formation energy (62)
Reactions on metals and SAAs	[56]	Activation energy (632) Reaction energy (632) Adsorbate formation energy (1481) TS formation energy (632)
Metal oxide nanoclusters	[58]	Zero-point energy (180)
Formate on metal oxide nanoclusters	[63]	Adsorption energy (2869)
Formate formation on metal oxide nanoclusters	[67]	Activation energy (144) Reaction energy (144)

extended OC20 [20, 35], ODAC25 [26], OMat24 [22], OMC25 [27], and OMol25 [28] data sets. In this study, we evaluated UMA performance for the OC20 and OMat24 tasks, using the small- and medium-size models, version 1.1 (UMA-S-1.1 and UMA-M-1.1). Furthermore, we also evaluated UMA performance for a UMA-M-1.1 model trained on OAM [22].

The AQCcat model family [29] contains models based on EquiformerV2, introducing additive shifts at various points in the model using feature-wise linear modulation (FiLM) [68]. These shifts incorporate task information on spin polarization treatment and fidelity. These models are trained on a combination of OC20 [20] and the AQCcat25 data set [29], which is an expansion of OC20 with explicit inclusion of spin polarization, which is used as a training feature. In this study, we evaluated AQCcat performance using the four publicly-available models.

The training data sets utilized to train the models discussed above were not all created equally; most importantly, they do not all use the same exchange-correlation functional. The MPTrj [30], OC22 [21], and OMat24 [22] data sets consist of a mixture of PBE [49] and PBE + U calculations, following Materials Project recommendations [69]. On the other hand, the Alex [24] (and thus sAlex [22]) and MatPES-PBE [23] data sets include only PBE calculations. The OC20 [20], OC25 [25], and AQCcat25 [29] data sets utilize the RPBE exchange-correlation functional [70]; the OC25 data set further applies a D3 correction with zero damping [71].

Because of the complexity of visualizing all evaluated MLIPs in figures, the MLIPs were divided into three dimensions for visualization: model family, indicated with color; training data set, indicated with markers; and model size (categorized into small, medium, and large), indicated with marker size. Not all MLIPs fit neatly within these dimensions, though, and some groups of distinct MLIPs have identical symbols under the scheme outlined above. Therefore, for these groups, only the best-performing MLIP (ranked by

RMSE) is shown in the figures. These groups are as follows: GemNet-OC with and without strict neighbor enforcement; SevenNet-0 and SevenNet-l3i5 trained on MPTrj; MACE-MP-0a (three sizes) and MACE-MP-0b3; Orb models with the same training data sets; and EquiformerV2-31M trained on MPTrj (with and without DeNS). The error values for all MLIPs, including the ones that are not shown in the figures, are available in the tables in Section S2.

2.4 Gas-phase error correction

Most target properties described above are calculated from purely solid-state geometries: bulks or slabs, possibly with adsorbates on top of these slabs. For example, the activation energy is the difference between the energy of the TS and the initial state of the reactants, adsorbed to the surface in both cases. Two exceptions exist to this: the formation energy (both for adsorbate and TS) and the adsorption energy. Both are calculated from a combination of solid-state and gas-phase geometries. However, all MLIPs investigated in this work target prediction of solid-state geometries and are trained with data sets containing only those geometries. Therefore, it cannot be expected that these MLIPs predict energies of gas-phase molecules with high accuracy. For a more fair comparison of MLIP accuracy, we present errors for the prediction of these properties after correcting the MLIP property predictions by the mean error across the entire set of predicted properties (except when indicated otherwise):

$$E_{\text{MLIP},i}^{\text{corr}} = E_{\text{MLIP},i} - \frac{1}{N} \sum_j (E_{\text{MLIP},j} - E_{\text{DFT},j}), \quad (9)$$

where $E_{\text{MLIP},i}$ is the MLIP-predicted energy value for property i , $E_{\text{DFT},i}$ is the DFT target value for property i , and N is the total number of property values. This offset is assumed to mostly comprise the error due to poor predictions of gas-phase geometries. Note that the correction value is calculated over the entire data set,

not split by molecule, as some molecules exist in very few data points and thus the error correction might not accurately reflect gas-phase prediction error.

In addition, the GemNet-dT model architecture cannot predict properties for systems with two atoms or less, and thus formation energies defined using Equation (2) (relying on the energy prediction of H_2 through Equation (3)) cannot be calculated with this architecture.

3 Results

3.1 Model performance trends

We begin by comparing the zero-shot performance of the different MLIPs for a subset of data sets and target properties, picking a number of interesting observations. This performance is quantified through the root mean square error (RMSE) and maximum absolute error (MaxAE) between the MLIP predictions and DFT energies. We again highlight that these results are a comparison of DFT-relaxed geometries, except when indicated otherwise. Furthermore, note that the DFT functional employed in the data sets used to train the foundational MLIPs (Section 2.3) may not match the functional used in the target property evaluation (Section 2.2). It is therefore possible that small changes to the ranking of the foundational MLIPs would occur if the target property were to be reevaluated with a different functional. Prediction performance for all MLIPs and all target properties is given in Section S2.

In Figure 2a, we show MLIP prediction performance for the slab vacancy formation energy of perovskite oxide surfaces. These results show that generally, the EquiformerV2, UMA, eSEN, and Orb model architectures are the most well-performing. However, a stronger trend is visible when analyzing model performance by training data sets. Models trained on OAM and OMat24 perform best, whereas models trained on OC20 clearly perform worst. This is unsurprising, given that the OMat24 data set includes inorganic bulk materials including many oxides, and thereby most closely approximates the perovskite oxide data set. On the other hand, OC20 does not feature oxide structures and focuses on adsorbates, which do not occur in this perovskite oxide data set. Some of the models trained on OC22, specifically aimed at covering metal oxide materials, perform reasonably well, but do not outperform those trained on OAM or OMat24.

This trend is much less obvious when analyzing MLIP performance for the formation energy of TSs of CO_2 hydrogenation reaction steps on (doped) $\text{ZrO}_2(101)$ surfaces, as shown in Figure 2b. A large spread can be observed for models trained on training data sets such as OAM and OMat24. Analogous to the previous example, eSEN, Orb and UMA are the best-performing models, while in this case the EquiformerV2 models are among the worst-performing models.

Trends are again different when analyzing the formation energy of TSs of RWGS reaction steps on metals and SAAs, as shown in Figure 2c. Here, the models

trained on the OC20, OC22, OC25, and even MPTrj data sets strongly outperform those trained on OAM and OMat24. A strong contributor here is that there is a large cluster of models—including models trained on OAM and OMat24—in the top right area of Figure 2c, showing very large prediction errors. This trend seems to be caused by poor prediction of magnetic elements, and is explored in more detail in the next section.

Overall, the training data set strongly affects model performance, possibly more so than the model architecture. The presence of oxide surfaces in the training data set seems to be more important in determining model performance than the presence of adsorbates. In fact, the zirconia data set shows that models trained on data sets not explicitly including adsorbates can still be highly performant for predicting TS energies of surface reactions. In general, we see that the eSEN, Orb, and UMA models (when combined with a suitable training data set) are the best-performing models from the set of models evaluated in this work.

3.2 Poor predictions of magnetic elements

One spurious observation is that a large number of MLIPs catastrophically fail to correctly predict formation energies of both reaction intermediates (Figure S8) and TSs (Figure 2c) on a large number of metal and SAA surfaces. As shown in these figures, many MLIPs exhibit RMSE values exceeding 3 eV, but more importantly maximum errors exceeding 15 eV, approaching 100 eV for the most extreme cases.

We further investigated these spurious errors by analyzing formation energy predictions split by surface and adsorbate (for reaction intermediates) and split by surface and reaction (for TSs). Some representative examples from this analysis are shown in Figures S15 and S16. Specifically, the combinations of C- and O-containing adsorbates on Co- and Ni-containing surfaces show large errors. In Figure 3, we show a comparison between RMSEs for the full data set and for the data set with Co- and Ni-containing surfaces removed. A subset of models clearly lies on or close to the parity line—indicating the Co- and Ni-containing surfaces do not significantly impact overall model performance—while many models show much larger RMSE values when Co- and Ni-containing surfaces are included. More specifically, the training data set-based trend discussed in the previous section is clearly visible in this figure. Models trained on OC20, OC22, and OC25 are most performant on Co- and Ni-containing surfaces, followed by models trained on MPTrj, and finally models trained on OMat24, Alex, or OAM show the largest errors. We hypothesize that this is caused by a combination of these materials being magnetic materials and the utilization of spin-polarization in the preparation of the training data sets. The CHGNet model shows the smallest discrepancy from the models trained on MPTrj; this could be due to its explicit inclusion of magnetic moments in training the model. Furthermore, the AQCAt models are very close to the parity line, which

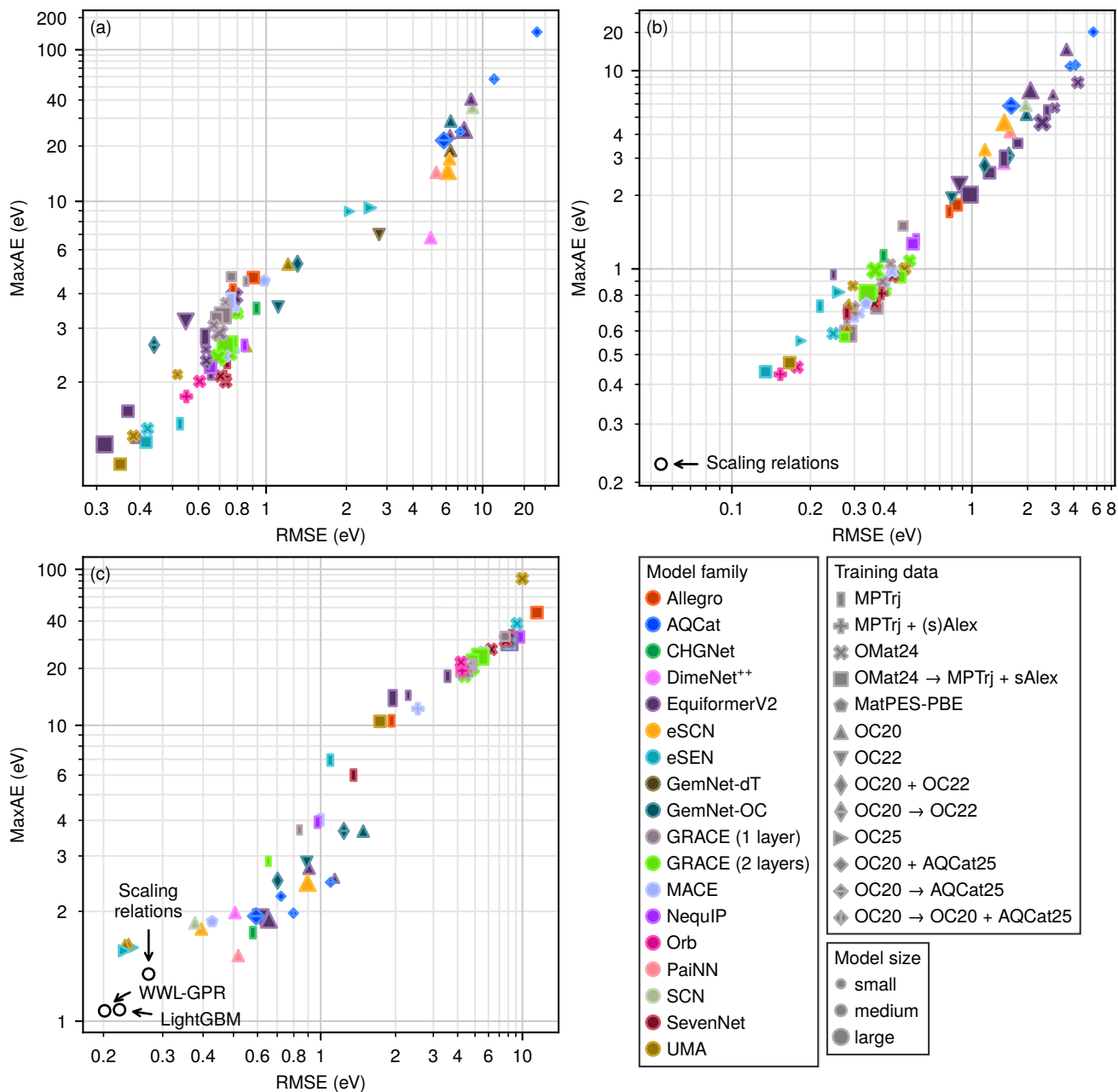


Figure 2: Prediction performance of the MLIPs for three different data sets and target properties: (a) slab vacancy formation energy of perovskite oxide surfaces; (b) formation energy of TSs of CO₂ hydrogenation reaction steps on (doped) ZrO₂(101) surfaces; (c) formation energy of TSs of RWGS reaction steps on metals and SAAs. Larger versions of these figures and data are available in Section S2.

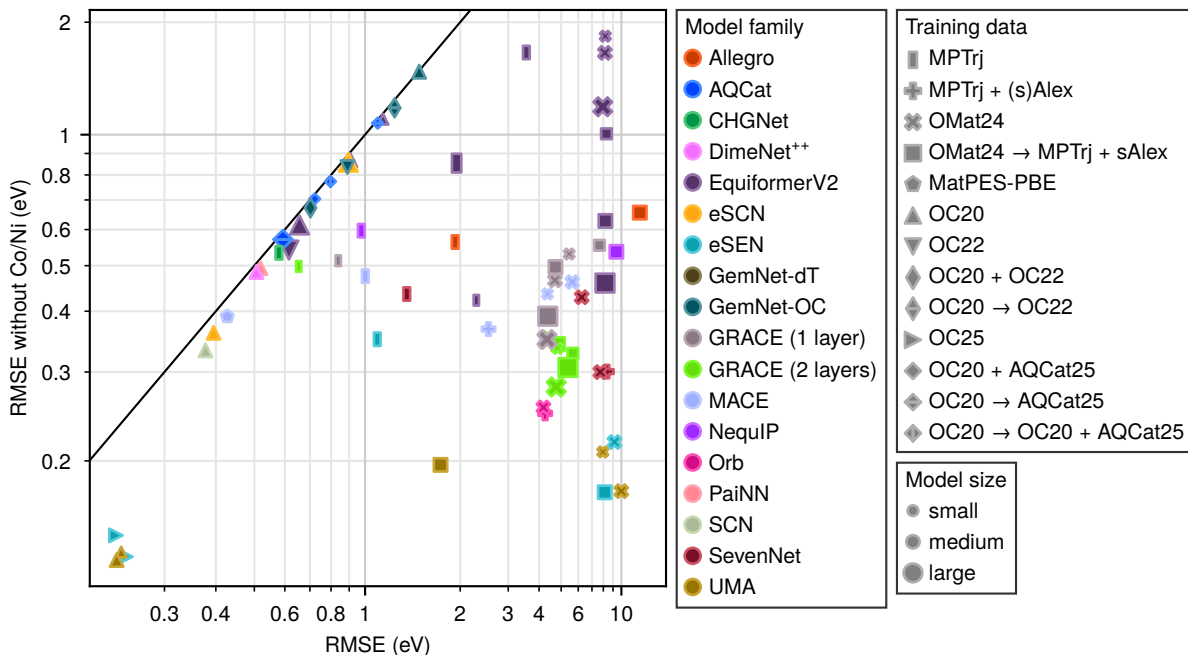


Figure 3: Comparison between RMSEs of formation energy predictions for TSs on metals and SAAs for the entire data set and for the data set with Co- and Ni-containing surfaces removed. The black line is a parity line. Data is available in Section S2.

might be due to its similar inclusion of spin polarization as an explicit feature at training and inference time. However, these models are trained on OC20 and derived data; it would be interesting to see how such a model architecture performs when trained on data derived from OMat24.

3.3 Vibrational modes

Calculating vibrational modes and their energies, via the Hessian, is crucial for determining free energies, for instance in the harmonic limit. However, approximating the Hessian using a finite difference approach requires $6N$ additional single-point calculations, where N is the number of atoms for which vibrational modes are to be determined. Therefore, it is common to evaluate vibrational modes for a subset of representative systems and use these to estimate modes for other systems [50, 56, 72].

Here, we analyzed MLIP performance for predicting vibrational modes using the finite difference approach, targeting the zero-point energy of metal-supported metal oxide nanoclusters as defined in Equation (7). To obtain accurate vibrational modes, MLIP relaxations were performed as discussed in Section 2.2.3. We also compare MLIP predictions to the linear fitting approach outlined by Reichenbach *et al.* [72] and applied to a similar data set.

The resulting comparison (Figure 4) shows that the majority of models can predict the zero-point energy with high accuracy, with approximately two-thirds of the evaluated models outperforming the linear fitting approach. This is in line with earlier work, showing good in-domain performance for the prediction of numerical Hessians using foundational MLIPs [73]. It

should be noted again that the choice of training data set is correlated with model performance, with models trained on data sets including inorganic materials (OMat24, OAM) generally outperforming models trained on catalysis-focused data sets (OC20, OC22), which are less closely related to the metal-supported metal oxide nanocluster data set. The eSEN and UMA models are the best performers, reaching RMSEs as low as 0.01 eV compared to the DFT-evaluated zero-point energies.

3.4 Relaxation in MLIPs

All comparisons between DFT results and MLIPs in Sections 3.1 and 3.2 have been performed by evaluating the energies of DFT-relaxed geometries. Realistic applications of MLIPs, however, would utilize the MLIP to perform relaxation. To explore this more realistic use case, we randomly sampled 10% of adsorption energies from the formate on metal oxide nanocluster data set, relaxed the corresponding adsorbed structures to a local minimum in each MLIP, and evaluated the resulting energy deviation from the DFT local minimum energy. The prediction performance for these relaxed structures is shown in Figure S12. A comparison between evaluations on the DFT local minima and evaluations on the MLIP local minima is shown in Figure 5. Generally, all models experience an increase in prediction error after relaxing into the MLIP local minima. For the best-performing models, this increase can be significant, with for instance the eSEN-30M model trained on OAM experiencing a $1.6\times$ increase in RMSE. More generally, a plateau is observed where RMSEs on the MLIP local minima do not reach below 0.18 eV, despite many models being capable of reaching these RMSE

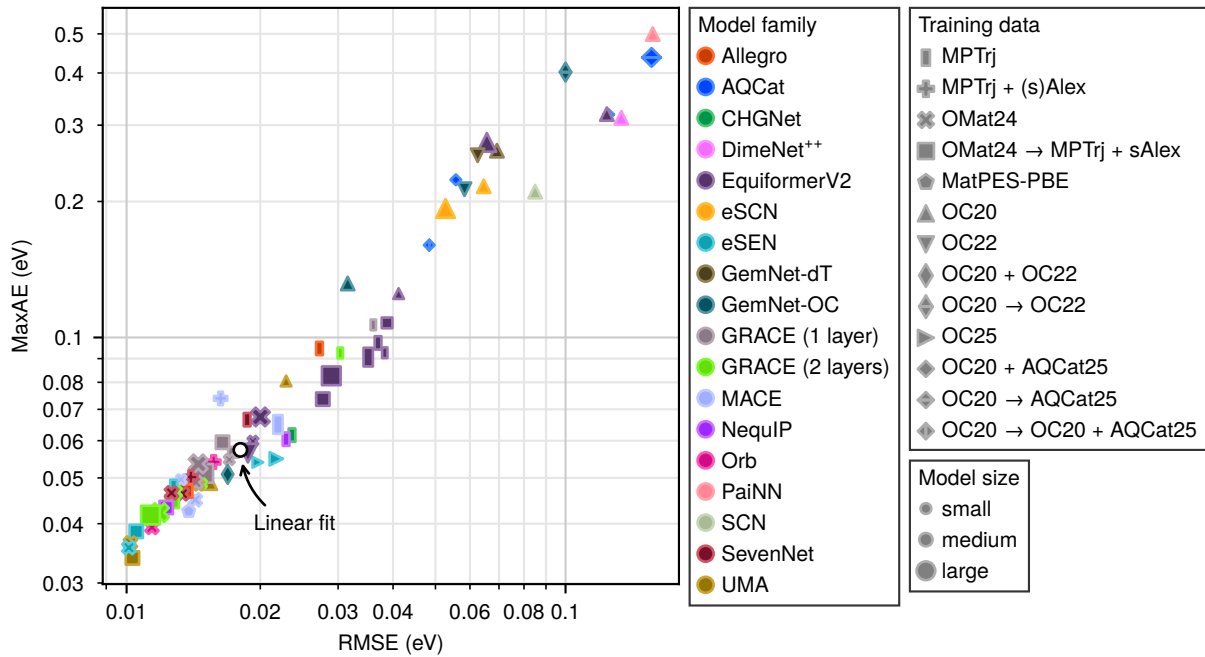


Figure 4: Prediction performance of the MLIPs for the zero-point energy of metal oxide nanoclusters on metal supports. The white circle indicates the linear fitting approach outlined by Reichenbach *et al.* [72]. Data is available in Section S2.

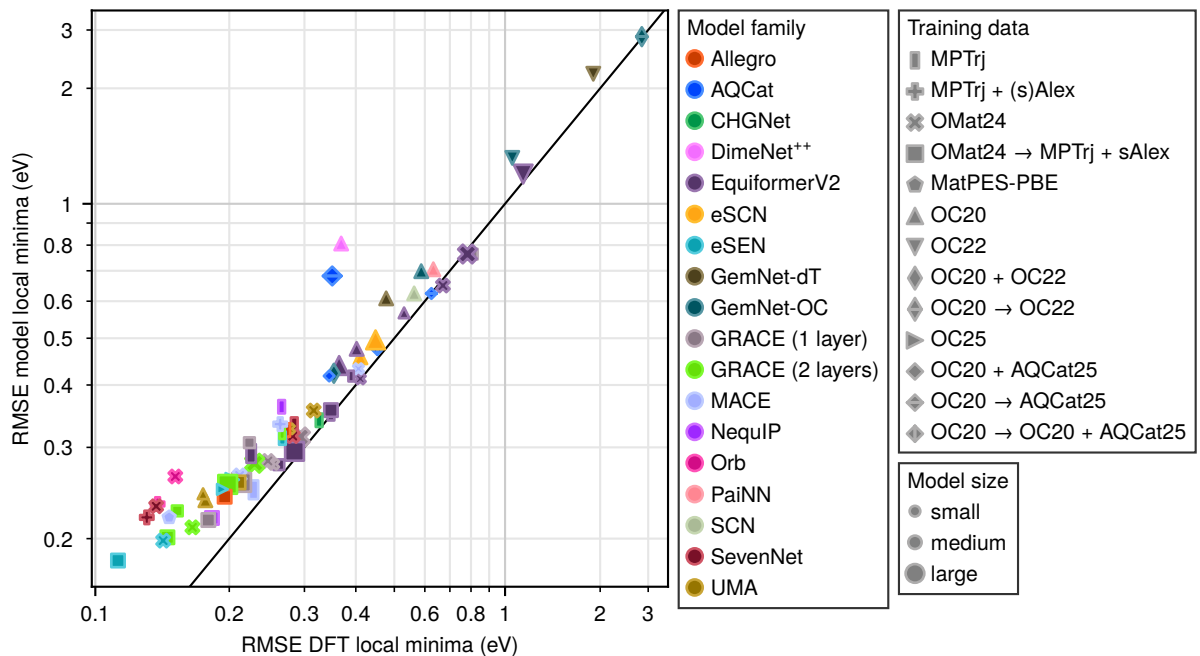


Figure 5: Comparison between RMSEs of adsorption energy predictions for formate on metal-supported oxide nanoclusters when evaluating the MLIP energy of the DFT local minimum and when relaxing into the MLIP local minimum and evaluating the energy of that structure. The black line is a parity line. Data is available in Section S2.

values on the DFT local minima.

3.5 Comparison to task-specific models

In contrast to foundational MLIPs, which target application across a wide range of data sets, task-specific models target much more specific applications, usually limited to the (much smaller) data set they have been trained on. In their respective papers, the data sets for reactions on alloyed metal and oxide surfaces and formate on metal-oxide interfaces have been used to train a range of task-specific models [50, 56, 63], targeting low-cost, direct prediction of formation energies of adsorbates and TSs. In this section, we compare performance from these models with that of the foundational MLIPs, giving an indication of the out-of-the-box quality of these MLIPs for catalyst applications compared to task-specific models.

It is important to note that the task-specific models discussed in this section are trained on the same DFT data sets on which their performance is evaluated. In contrast, the errors reported for the MLIPs are obtained using the models out-of-the-box, without any fine-tuning to the DFT datasets considered here (correcting only for the gas-phase reference when applicable as described in Section 2.4).

The first set of task-specific models we analyze is the linear scaling relations derived by Cheula *et al.* [50] for the formation energy of TSs of CO₂ hydrogenation reaction steps on (doped) ZrO₂(101) surfaces. These relations are linear fits of the formation energies of TSs to those of related reaction intermediates. In Figure 2b, we highlight their accuracy with a white circle. The error reported is a training error. However, owing to the simplicity of the linear fit, test errors are typically rather similar to training errors. The figure shows that these scaling relations are substantially more accurate than the foundational MLIPs; approximately 3 times as accurate as the best-performing model. However, it should be noted that scaling relations are very limited in their applicability, as a different relation is used to describe each reaction step.

Next, we analyze the set of models derived by Cheula & Andersen [56] for the formation energies of both adsorbates and TSs on metals and SAAs. These models include scaling relations, ensemble decision tree models (LightGBM), and graph kernel-based Gaussian Process Regression (WWL-GPR) models. We highlight the errors of these models (determined via 5-fold cross-validation) in Figure S8 for adsorbates and in Figure 2c for TSs. Differences between the task-specific models are discussed in more detail by Cheula & Andersen [56], so they are not discussed further here. The figures show that for adsorbates, the task-specific models show better or similar performance as that of the UMA MLIPs, which are the best-performing MLIPs for this property. For TSs, the task-specific models (with the exception of the simplest model, the scaling relations) show better performance than the eSEN and UMA MLIPs, especially regarding the maximum error predicted by the models. Here it is also important to note that—similar

to the observation for the formate on metal oxide nanocluster data set in Figure 5—relaxation in the MLIP may increase the error of the best-performing MLIPs.

Finally, we analyze the set of models derived by Nielsen *et al.* [63] for the adsorption energies of formate on metal-supported metal oxide nanoclusters. The derived models offer a range of physical interpretability, and include RBF-GPR, XGBoost, SISSO, and WWL-GPR. The errors of these models are highlighted in Figures S11 and S12 for the comparison between evaluations on the DFT local minima and on the MLIP local minima, respectively (see Section 3.4). Differences between the task-specific models are discussed in more detail by Nielsen *et al.* [63], so they are not discussed further here. Focusing first on the comparison with DFT local minima (Figure S11), we see the cluster of best-performing MLIPs outperforming the task-specific models, achieving up to twice as good RMSE performance. However, as discussed in Section 3.4, the best-performing MLIPs are most strongly affected by MLIP relaxation. Hence, the picture changes when focusing on the comparison with MLIP local minima (Figure S12). In this case, the task-specific models are much more performant compared to the MLIPs; the best-performing models even outperforming the best MLIPs.

In general, the task-specific models discussed above outperform the foundational MLIPs in all cases, although the differences are quite slim in some cases, and in the final example the models only outperformed MLIPs when comparing against MLIP local minima.

It is worth highlighting that the task-specific models predict properties for relaxed geometries using feature inputs only determined from non-relaxed geometries—the clean surfaces and information regarding the adsorption motif. Therefore, applying these models is significantly cheaper and easier than applying a foundational MLIP for obtaining a property value, as the latter requires creating an adsorption geometry and relaxing this geometry. However, it should also be reiterated that the task-specific models have limited applicability, and the nature of their construction means they cannot be compared one-to-one to foundational MLIPs. This is discussed in more detail in the next section.

4 Discussion

In this work, we have systematically evaluated zero-shot performance of 80 different pretrained MLIPs on 13 properties relevant to heterogeneous catalysis, across 6 different data sets, obtaining over 700 000 potential energy evaluations. Our findings show that there is a large spread of accuracy between the different MLIPs, but more importantly, that there is no singular MLIP that is universally the best-performing model. The best-performing MLIP differs between the different data sets evaluated in this work, but also differs between target properties within the same data set (i.e., reaction energy and adsorbate formation energy). It is therefore imperative that one carefully investigates which foundational MLIP is most suitable for the desired application, as there is no generically applicable answer to

this question. Based on the findings in this work, the eSEN, Orb, and UMA models seem to be among the best-performing models across most of the evaluated properties. Therefore, it is recommended to use these as a starting point for exploring model performance.

For the properties based on an energy difference (all except for zero-point energy), we observe that the best models can be very accurate, with RMSEs generally on the order of 0.1–0.3 eV and maximum errors on the order of 0.2–2 eV. In this comparison, it is important to keep in mind that both the DFT data sets that the foundational MLIPs have been trained on and the catalysis-related data sets assembled in this work have been obtained with different DFT functionals and numerical settings. Furthermore, depending on the property of interest, commonly used DFT functionals may have a sizable intrinsic error compared to experiments. For instance, one study focusing on surface reaction energies found that functionals such as PBE, RPBE and BEEF-vdW may exhibit errors around 0.2–0.3 eV or larger relative to experiment [74]. Nevertheless, we are not yet at a point where the additional error introduced by replacing DFT with a foundational MLIP is negligible compared to the intrinsic DFT error. Therefore, caution is suggested when using MLIP results for further analysis (i.e., microkinetic models based on activation energies). However, the current-generation MLIPs are more than accurate enough for initial screening purposes, i.e., to approximate a desired property value, narrowing down a large amount of candidates into a smaller set, which can then be evaluated more accurately with suitable DFT settings. Furthermore, it can be expected that MLIP accuracy will continue to increase in the coming years.

In addition to comparing foundational MLIPs to each other, we also compared them to a range of task-specific models trained on the specific data sets explored in this work. These models include simple linear scaling relations, more advanced graph-based GPR models, and decision tree models. We show that these models can compete with the current generation of best-performing MLIPs. However, it is important to note that differences in their construction to that of MLIPs mean that they are not equally easy to apply. Crucially, training task-specific models requires knowing DFT energies for relevant geometries *a priori*, which is usually time-consuming and, in case of for example TS determination, nontrivial. The task-specific models explored in this work have been trained on a large subset of the full data sets, whereas the foundational MLIPs have been trained on none of the geometries evaluated in this work. It is therefore impressive that current-generation foundational MLIPs can obtain accuracy to this order of magnitude. They achieve this due to their immense size—and the immense size of the training data sets—which is also a disadvantage, as inference times of MLIPs are much larger than those of the much simpler task-specific models. Furthermore, some of the task-specific models (i.e., XGBoost and SISSO) offer model interpretability, providing insight in the underlying structure–property correlations [63]. The founda-

tional MLIPs, by virtue of being immensely large graph neural networks, are entirely black-box models and can offer none of this interpretability.

One area of foundational MLIP application unexplored in this work, which can bridge the gap between DFT and MLIP performance described above, is augmentation of pretrained MLIPs, such as fine-tuning or Δ -learning. In fine-tuning, training of an MLIP is continued with a different data set, which more closely approximates the target application of the MLIP. Fine-tuning is already applied as part of the training protocol of many foundational MLIPs such as Orb [34, 75], eSEN [19], and UMA [35], where the large training data sets discussed in Section 2.3 are utilized. However, fine-tuning can also be applied downstream using a small data set, with the goal of obtaining a model that is more accurate specifically in the region of this data set, and where loss of general performance is acceptable. This type of fine-tuning has been successfully applied to a wide range of problems, from more general problems such as correcting for softening in MLIPs [76] to more specific materials science applications [77–81]. In the Δ -learning approach [82], a machine learning model is trained with the goal to accurately predict the error between a baseline calculation and the target calculation, such that the output of this model can be added to the baseline calculation to more closely approximate the target value. In the context of MLIPs, the baseline calculation is the foundational MLIP prediction. Here, Δ -learning has been successfully applied to a range of different materials science applications [78, 83, 84], although it has also been shown to not always be competitive with training an MLIP from scratch [80]. Overall, augmentation of foundational MLIPs can be a powerful method of training highly accurate, but less general, custom potentials for specific applications. However, the approaches discussed above require initial collection of a training data set suitable for the desired application, which introduces similar disadvantages to those observed with the use of task-specific models. Additionally, the question of which data to include in such a training data set—both in terms of data set size as well as coverage of the parameter space—is nontrivial. Furthermore, many hyperparameters and workflow choices are involved in setting up a fine-tuning or Δ -learning workflow, which can all impact the quality of the resulting model. As pretrained MLIPs generally consist of millions of parameters, the computational resources required to fine-tune a pretrained MLIP can also be high, even if the fine-tuning data set is relatively small—especially when some sort of hyperparameter optimization is additionally performed. In short, the above reasons mean zero-shot application of a pretrained MLIP is much more desirable than augmentation, although the current-generation pretrained MLIPs are not quite yet at the accuracy required for this to be fully feasible across all applications.

Supplementary material

Overview of evaluated MLIPs, model training performance (figures and tables) for all properties, and additional figures on poor prediction of magnetic elements.

Acknowledgments

The authors would like to acknowledge funding from VILLUM FONDEN (grant no. 37381), Novo Nordisk Fonden (grant no. NNF22OC0078939) and the Danish National Research Foundation through the Center of Excellence ‘InterCat’ (grant no. DNRF150). Computational support was provided by the Centre for Scientific Computing Aarhus (CSCAA) at Aarhus University.

Author declarations

Conflict of interest

The authors have no conflicts to disclose.

Author contributions

Luuk H. E. Kempen: Conceptualization (equal); Investigation (lead); Methodology (lead); Software (lead); Visualization (lead), Writing – original draft (lead); Writing – review & editing (equal). **Raffaele Cheula:** Investigation (supporting); Visualization (supporting); Writing – review & editing (equal). **Mie Andersen:** Conceptualization (equal); Investigation (supporting); Writing – review & editing (equal); Supervision (lead); Resources (lead); Funding acquisition (lead).

Data availability

The data that support the findings of this study will be made available on Zenodo upon publication under a CC BY 4.0 license.

Code availability

The source code will be made available on GitLab upon publication under a GNU GPLv3 license.

References

1. Kulichenko, M. *et al.* Data Generation for Machine Learning Interatomic Potentials and Beyond. *Chemical Reviews* **124**, 13681–13714. ISSN: 1520-6890. <http://dx.doi.org/10.1021/acs.chemrev.4c00572> (2024).
2. Choi, J., Nam, G., Choi, J. & Jung, Y. A Perspective on Foundation Models in Chemistry. *JACS Au* **5**, 1499–1518. ISSN: 2691-3704. <http://dx.doi.org/10.1021/jacsau.4c01160> (2025).
3. Omranpour, A., Elsner, J., Lausch, K. N. & Behler, J. Machine Learning Potentials for Heterogeneous Catalysis. *ACS Catalysis* **15**, 1616–1634. ISSN: 2155-5435. <http://dx.doi.org/10.1021/acscatal.4c06717> (2025).
4. Schütt, K. T., Unke, O. T. & Gastegger, M. *Equivariant message passing for the prediction of tensorial properties and molecular spectra* 2021. arXiv: 2102.03150 [cs.LG]. <https://arxiv.org/abs/2102.03150>.
5. Gasteiger, J., Giri, S., Margraf, J. T. & Günnemann, S. *Fast and Uncertainty-Aware Directional Message Passing for Non-Equilibrium Molecules* 2022. arXiv: 2011.14115 [cs.LG]. <https://arxiv.org/abs/2011.14115>.
6. Gasteiger, J., Becker, F. & Günnemann, S. *GemNet: Universal Directional Graph Neural Networks for Molecules* 2024. arXiv: 2106.08903 [physics.comp-ph]. <https://arxiv.org/abs/2106.08903>.
7. Gasteiger, J. *et al.* *GemNet-OC: Developing Graph Neural Networks for Large and Diverse Molecular Simulation Datasets* 2022. arXiv: 2204.02782 [cs.LG]. <https://arxiv.org/abs/2204.02782>.
8. Batzner, S. *et al.* E(3)-equivariant graph neural networks for data-efficient and accurate interatomic potentials. *Nature Communications* **13**, 2453. ISSN: 2041-1723. <http://dx.doi.org/10.1038/s41467-022-29939-5> (2022).
9. Tan, C. W. *et al.* *High-performance training and inference for deep equivariant interatomic potentials* 2025. arXiv: 2504.16068 [physics.comp-ph]. <https://arxiv.org/abs/2504.16068>.
10. Musaelian, A. *et al.* Learning local equivariant representations for large-scale atomistic dynamics. *Nature Communications* **14**, 579. ISSN: 2041-1723. <http://dx.doi.org/10.1038/s41467-023-36329-y> (2023).
11. Park, Y., Kim, J., Hwang, S. & Han, S. Scalable Parallel Algorithm for Graph Neural Network Interatomic Potentials in Molecular Dynamics Simulations. *Journal of Chemical Theory and Computation* **20**, 4857–4868. ISSN: 1549-9626. <http://dx.doi.org/10.1021/acs.jctc.4c00190> (2024).
12. Batatia, I., Kovács, D. P., Simm, G. N. C., Ortner, C. & Csányi, G. *MACE: Higher Order Equivariant Message Passing Neural Networks for Fast and Accurate Force Fields* 2023. arXiv: 2206.07697 [stat.ML]. <https://arxiv.org/abs/2206.07697>.
13. Bochkarev, A., Lysogorskiy, Y. & Drautz, R. Graph Atomic Cluster Expansion for Semilocal Interactions beyond Equivariant Message Passing. *Physical Review X* **14**, 021036. ISSN: 2160-3308. <http://dx.doi.org/10.1103/PhysRevX.14.021036> (2024).

14. Zitnick, C. L. *et al.* *Spherical Channels for Modeling Atomic Interactions* 2022. arXiv: 2206.14331 [physics.chem-ph]. <https://arxiv.org/abs/2206.14331>.
15. Passaro, S. & Zitnick, C. L. *Reducing $SO(3)$ Convolutions to $SO(2)$ for Efficient Equivariant GNNs* 2023. arXiv: 2302.03655 [cs.LG]. <https://arxiv.org/abs/2302.03655>.
16. Liao, Y.-L. & Smidt, T. *Equiformer: Equivariant Graph Attention Transformer for 3D Atomistic Graphs* 2023. arXiv: 2206.11990 [cs.LG]. <https://arxiv.org/abs/2206.11990>.
17. Liao, Y.-L., Wood, B., Das, A. & Smidt, T. *EquiformerV2: Improved Equivariant Transformer for Scaling to Higher-Degree Representations* 2024. arXiv: 2306.12059 [cs.LG]. <https://arxiv.org/abs/2306.12059>.
18. Liao, Y.-L., Smidt, T., Shuaibi, M. & Das, A. *Generalizing Denoising to Non-Equilibrium Structures Improves Equivariant Force Fields* 2024. arXiv: 2403.09549 [cs.LG]. <https://arxiv.org/abs/2403.09549>.
19. Fu, X. *et al.* *Learning Smooth and Expressive Interatomic Potentials for Physical Property Prediction* 2025. arXiv: 2502.12147 [physics.comp-ph]. <https://arxiv.org/abs/2502.12147>.
20. Chanussot, L. *et al.* Open Catalyst 2020 (OC20) Dataset and Community Challenges. *ACS Catalysis* **11**, 6059–6072. ISSN: 2155-5435. <http://dx.doi.org/10.1021/acscatal.0c04525> (2021).
21. Tran, R. *et al.* The Open Catalyst 2022 (OC22) Dataset and Challenges for Oxide Electrocatalysts. *ACS Catalysis* **13**, 3066–3084. ISSN: 2155-5435. <http://dx.doi.org/10.1021/acscatal.2c05426> (2023).
22. Barroso-Luque, L. *et al.* *Open Materials 2024 (OMat24) Inorganic Materials Dataset and Models* 2024. arXiv: 2410.12771 [cond-mat.mtrl-sci]. <https://arxiv.org/abs/2410.12771>.
23. Kaplan, A. D. *et al.* *A Foundational Potential Energy Surface Dataset for Materials* 2025. arXiv: 2503.04070 [cond-mat.mtrl-sci]. <https://arxiv.org/abs/2503.04070>.
24. Schmidt, J. *et al.* Machine-Learning-Assisted Determination of the Global Zero-Temperature Phase Diagram of Materials. *Advanced Materials* **35**, 2210788. ISSN: 1521-4095. <http://dx.doi.org/10.1002/adma.202210788> (2023).
25. Sahoo, S. J. *et al.* *The Open Catalyst 2025 (OC25) Dataset and Models for Solid-Liquid Interfaces* 2025. arXiv: 2509.17862 [cond-mat.mtrl-sci]. <https://arxiv.org/abs/2509.17862>.
26. Sriram, A. *et al.* *The Open DAC 2025 Dataset for Sorbent Discovery in Direct Air Capture* 2025. arXiv: 2508.03162 [cond-mat.mtrl-sci]. <https://arxiv.org/abs/2508.03162>.
27. Gharakhanyan, V. *et al.* *Open Molecular Crystals 2025 (OMC25) Dataset and Models* 2025. arXiv: 2508.02651 [physics.chem-ph]. <https://arxiv.org/abs/2508.02651>.
28. Levine, D. S. *et al.* *The Open Molecules 2025 (OMol25) Dataset, Evaluations, and Models* 2025. arXiv: 2505.08762 [physics.chem-ph]. <https://arxiv.org/abs/2505.08762>.
29. Allam, O., Wander, B. & Singh, A. R. *AQCat25: Unlocking spin-aware, high-fidelity machine learning potentials for heterogeneous catalysis* 2025. arXiv: 2510.22938 [cond-mat.mtrl-sci]. <https://arxiv.org/abs/2510.22938>.
30. Deng, B. *et al.* CHGNet as a pretrained universal neural network potential for charge-informed atomistic modelling. *Nature Machine Intelligence* **5**, 1031–1041. ISSN: 2522-5839. <http://dx.doi.org/10.1038/s42256-023-00716-3> (2023).
31. Batatia, I. *et al.* A foundation model for atomistic materials chemistry. *The Journal of Chemical Physics* **163**, 184110. ISSN: 1089-7690. <http://dx.doi.org/10.1063/5.0297006> (2025).
32. Kim, J. *et al.* Data-Efficient Multifidelity Training for High-Fidelity Machine Learning Interatomic Potentials. *Journal of the American Chemical Society* **147**, 1042–1054. ISSN: 1520-5126. <http://dx.doi.org/10.1021/jacs.4c14455> (2024).
33. Lysogorskiy, Y., Bochkarev, A. & Drautz, R. *Graph atomic cluster expansion for foundational machine learning interatomic potentials* 2025. arXiv: 2508.17936 [cond-mat.mtrl-sci]. <https://arxiv.org/abs/2508.17936>.
34. Rhodes, B. *et al.* *Orb-v3: atomistic simulation at scale* 2025. arXiv: 2504.06231 [cond-mat.mtrl-sci]. <https://arxiv.org/abs/2504.06231>.
35. Wood, B. M. *et al.* *UMA: A Family of Universal Models for Atoms* 2025. arXiv: 2506.23971 [cs.LG]. <https://arxiv.org/abs/2506.23971>.
36. Goldsmith, B. R., Peters, B., Johnson, J. K., Gates, B. C. & Scott, S. L. Beyond Ordered Materials: Understanding Catalytic Sites on Amorphous Solids. *ACS Catalysis* **7**, 7543–7557. ISSN: 2155-5435. <http://dx.doi.org/10.1021/acscatal.7b01767> (2017).
37. Chee, S. W., Lunkenbein, T., Schlögl, R. & Roldán Cuenya, B. *Operando* Electron Microscopy of Catalysts: The Missing Cornerstone in Heterogeneous Catalysis Research? *Chemical Reviews* **123**, 13374–13418. ISSN: 1520-6890. <http://dx.doi.org/10.1021/acs.chemrev.3c00352> (2023).
38. Riebesell, J. *et al.* A framework to evaluate machine learning crystal stability predictions. *Nature Machine Intelligence* **7**, 836–847. ISSN: 2522-5839. <http://dx.doi.org/10.1038/s42256-025-01055-1> (2025).

39. Schaaf, L. L., Fako, E., De, S., Schäfer, A. & Csányi, G. Accurate energy barriers for catalytic reaction pathways: an automatic training protocol for machine learning force fields. *npj Computational Materials* **9**, 180. ISSN: 2057-3960. <http://dx.doi.org/10.1038/s41524-023-01124-2> (2023).
40. Perego, S. & Bonati, L. Data efficient machine learning potentials for modeling catalytic reactivity via active learning and enhanced sampling. *npj Computational Materials* **10**, 291. ISSN: 2057-3960. <http://dx.doi.org/10.1038/s41524-024-01481-6> (2024).
41. Yang, C., Wu, C., Xie, W., Xie, D. & Hu, P. General reactive element-based machine learning potentials for heterogeneous catalysis. *Nature Catalysis* **8**, 891–904. ISSN: 2520-1158. <http://dx.doi.org/10.1038/s41929-025-01398-3> (2025).
42. Andersen, M., Panosetti, C. & Reuter, K. A Practical Guide to Surface Kinetic Monte Carlo Simulations. *Frontiers in Chemistry* **7**, 202. ISSN: 2296-2646. <http://dx.doi.org/10.3389/fchem.2019.00202> (2019).
43. Motagamwala, A. H. & Dumesic, J. A. Microkinetic Modeling: A Tool for Rational Catalyst Design. *Chemical Reviews* **121**, 1049–1076. ISSN: 1520-6890. <http://dx.doi.org/10.1021/acs.chemrev.0c00394> (2021).
44. Hjorth Larsen, A. *et al.* The atomic simulation environment—a Python library for working with atoms. *Journal of Physics: Condensed Matter* **29**, 273002. ISSN: 1361-648X. <http://dx.doi.org/10.1088/1361-648x/aa680e> (2017).
45. Taylor, N. T., Morgan, M. T. & Hepplestone, S. P. Instability of ABO_3 perovskite surfaces induced by vacancy formation ($A = \text{Ca, Sr, Ba}$; $B = \text{Ti, Zr, Sn}$). *Physical Review B* **112**, 045308. ISSN: 2469-9969. <http://dx.doi.org/10.1103/w683-tvc4> (2025).
46. Kresse, G. & Furthmüller, J. Efficiency of *ab-initio* total energy calculations for metals and semiconductors using a plane-wave basis set. *Computational Materials Science* **6**, 15–50. ISSN: 0927-0256. [http://dx.doi.org/10.1016/0927-0256\(96\)00008-0](http://dx.doi.org/10.1016/0927-0256(96)00008-0) (1996).
47. Kresse, G. & Furthmüller, J. Efficient iterative schemes for *ab initio* total-energy calculations using a plane-wave basis set. *Physical Review B* **54**, 11169–11186. ISSN: 1095-3795. <http://dx.doi.org/10.1103/PhysRevB.54.11169> (1996).
48. Blöchl, P. E. Projector augmented-wave method. *Physical Review B* **50**, 17953–17979. ISSN: 1095-3795. <http://dx.doi.org/10.1103/physrevb.50.17953> (1994).
49. Perdew, J. P., Burke, K. & Ernzerhof, M. Generalized Gradient Approximation Made Simple. *Physical Review Letters* **77**, 3865–3868. ISSN: 1079-7114. <http://dx.doi.org/10.1103/physrevlett.77.3865> (1996).
50. Cheula, R., Tran, T. A. M. Q. & Andersen, M. Unraveling the Effect of Dopants in Zirconia-Based Catalysts for CO_2 Hydrogenation to Methanol. *ACS Catalysis* **14**, 13126–13135. ISSN: 2155-5435. <http://dx.doi.org/10.1021/acscatal.4c03206> (2024).
51. Giannozzi, P. *et al.* QUANTUM ESPRESSO: a modular and open-source software project for quantum simulations of materials. *Journal of Physics: Condensed Matter* **21**, 395502. ISSN: 1361-648X. <http://dx.doi.org/10.1088/0953-8984/21/39/395502> (2009).
52. Giannozzi, P. *et al.* Advanced capabilities for materials modelling with QUANTUM ESPRESSO. *Journal of Physics: Condensed Matter* **29**, 465901. ISSN: 1361-648X. <http://dx.doi.org/10.1088/1361-648X/aa8f79> (2017).
53. Prandini, G., Marrazzo, A., Castelli, I. E., Mounet, N. & Marzari, N. *A Standard Solid State Pseudopotentials (SSSP) library optimized for precision and efficiency (Version 1.1, data download)* 2018. <https://archive.materialscloud.org/doi/10.24435/materialscloud:2018.0001/v3>.
54. Anisimov, V. I., Zaanen, J. & Andersen, O. K. Band theory and Mott insulators: Hubbard U instead of Stoner I . *Physical Review B* **44**, 943–954. ISSN: 1095-3795. <http://dx.doi.org/10.1103/PhysRevB.44.943> (1991).
55. Cococcioni, M. & de Gironcoli, S. Linear response approach to the calculation of the effective interaction parameters in the LDA + U method. *Physical Review B* **71**, 035105. ISSN: 1550-235X. <http://dx.doi.org/10.1103/PhysRevB.71.035105> (2005).
56. Cheula, R. & Andersen, M. Transition States Energies from Machine Learning: An Application to Reverse Water–Gas Shift on Single-Atom Alloys. *ACS Catalysis* **15**, 11377–11388. ISSN: 2155-5435. <http://dx.doi.org/10.1021/acscatal.5c02818> (2025).
57. Wellendorff, J. *et al.* Density functionals for surface science: Exchange–correlation model development with Bayesian error estimation. *Physical Review B* **85**, 235149. ISSN: 1550-235X. <http://dx.doi.org/10.1103/PhysRevB.85.235149> (2012).
58. Kempen, L. H. E. & Andersen, M. Inverse catalysts: tuning the composition and structure of oxide clusters through the metal support. *npj Computational Materials* **11**, 8. ISSN: 2057-3960. <http://dx.doi.org/10.1038/s41524-024-01507-z> (2025).
59. Mortensen, J. J., Hansen, L. B. & Jacobsen, K. W. Real-space grid implementation of the projector augmented wave method. *Physical Review B* **71**, 035109. ISSN: 1550-235X. <http://dx.doi.org/10.1103/physrevb.71.035109> (2005).

60. Enkovaara, J. *et al.* Electronic structure calculations with GPAW: a real-space implementation of the projector augmented-wave method. *Journal of Physics: Condensed Matter* **22**, 253202. ISSN: 1361-648X. <http://dx.doi.org/10.1088/0953-8984/22/25/253202> (2010).
61. Mortensen, J. J. *et al.* GPAW: An open Python package for electronic structure calculations. *The Journal of Chemical Physics* **160**, 092503. ISSN: 1089-7690. <http://dx.doi.org/10.1063/5.0182685> (2024).
62. Monkhorst, H. J. & Pack, J. D. Special points for Brillouin-zone integrations. *Physical Review B* **13**, 5188–5192. ISSN: 0556-2805. <http://dx.doi.org/10.1103/physrevb.13.5188> (1976).
63. Nielsen, M. J., Kempen, L. H. E., de Neergaard Ravn, J., Cheula, R. & Andersen, M. Interpretable machine learned predictions of adsorption energies at the metal–oxide interface. *The Journal of Chemical Physics* **163**, 044708. ISSN: 1089-7690. <http://dx.doi.org/10.1063/5.0282674> (2025).
64. Caldeweyher, E., Bannwarth, C. & Grimme, S. Extension of the D3 dispersion coefficient model. *The Journal of Chemical Physics* **147**, 034112. ISSN: 1089-7690. <http://dx.doi.org/10.1063/1.4993215> (2017).
65. Caldeweyher, E. *et al.* A generally applicable atomic-charge dependent London dispersion correction. *The Journal of Chemical Physics* **150**, 154122. ISSN: 1089-7690. <http://dx.doi.org/10.1063/1.5090222> (2019).
66. Caldeweyher, E., Mewes, J.-M., Ehlert, S. & Grimme, S. Extension and evaluation of the D4 London-dispersion model for periodic systems. *Physical Chemistry Chemical Physics* **22**, 8499–8512. ISSN: 1463-9084. <http://dx.doi.org/10.1039/d0cp00502a> (2020).
67. Kempen, L. H. E., Nielsen, M. J. & Andersen, M. Breaking Scaling Relations with Inverse Catalysts: A Machine Learning Exploration of Trends in CO₂-to-Formate Energy Barriers. *ACS Catalysis* **15**, 17635–17644. ISSN: 2155-5435. <http://dx.doi.org/10.1021/acscatal.5c05872> (2025).
68. Perez, E., Strub, F., De Vries, H., Dumoulin, V. & Courville, A. FiLM: Visual Reasoning with a General Conditioning Layer. *Proceedings of the AAAI Conference on Artificial Intelligence* **32**, 3942–3951. ISSN: 2159-5399. <http://dx.doi.org/10.1609/aaai.v32i1.11671> (2018).
69. Jain, A. *et al.* Commentary: The Materials Project: A materials genome approach to accelerating materials innovation. *APL Materials* **1**, 011002. ISSN: 2166-532X. <http://dx.doi.org/10.1063/1.4812323> (2013).
70. Hammer, B., Hansen, L. B. & Nørskov, J. K. Improved adsorption energetics within density-functional theory using revised Perdew–Burke–Ernzerhof functionals. *Physical Review B* **59**, 7413–7421. ISSN: 1095-3795. <http://dx.doi.org/10.1103/PhysRevB.59.7413> (1999).
71. Grimme, S., Antony, J., Ehrlich, S. & Krieg, H. A consistent and accurate *ab initio* parametrization of density functional dispersion correction (DFT-D) for the 94 elements H–Pu. *The Journal of Chemical Physics* **132**, 154104. ISSN: 1089-7690. <http://dx.doi.org/10.1063/1.3382344> (2010).
72. Reichenbach, T., Walter, M., Moseler, M., Hammer, B. & Bruix, A. Effects of Gas-Phase Conditions and Particle Size on the Properties of Cu(111)-Supported Zn_yO_x Particles Revealed by Global Optimization and Ab Initio Thermodynamics. *The Journal of Physical Chemistry C* **123**, 30903–30916. ISSN: 1932-7455. <http://dx.doi.org/10.1021/acs.jpcc.9b07715> (2019).
73. Wander, B., Musielewicz, J., Cheula, R. & Kitchin, J. R. Accessing Numerical Energy Hessians with Graph Neural Network Potentials and Their Application in Heterogeneous Catalysis. *The Journal of Physical Chemistry C* **129**, 3510–3521. ISSN: 1932-7455. <http://dx.doi.org/10.1021/acs.jpcc.4c07477> (2025).
74. Wellendorff, J. *et al.* A benchmark database for adsorption bond energies to transition metal surfaces and comparison to selected DFT functionals. *Surface Science* **640**, 36–44. ISSN: 0039-6028. <http://dx.doi.org/10.1016/j.susc.2015.03.023> (2015).
75. Neumann, M. *et al.* Orb: A Fast, Scalable Neural Network Potential 2024. arXiv: 2410.22570 [cond-mat.mtrl-sci]. <https://arxiv.org/abs/2410.22570>.
76. Deng, B. *et al.* Overcoming systematic softening in universal machine learning interatomic potentials by fine-tuning 2024. arXiv: 2405.07105 [cond-mat.mtrl-sci]. <https://arxiv.org/abs/2405.07105>.
77. Kaur, H. *et al.* Data-efficient fine-tuning of foundational models for first-principles quality sublimation enthalpies. *Faraday Discussions* **256**, 120–138. ISSN: 1364-5498. <http://dx.doi.org/10.1039/D4FD00107A> (2025).
78. Pitfield, J. *et al.* Augmentation of Universal Potentials for Broad Applications. *Physical Review Letters* **134**, 056201. ISSN: 1079-7114. <http://dx.doi.org/10.1103/PhysRevLett.134.056201> (2025).
79. Della Pia, F. *et al.* Accurate and efficient machine learning interatomic potentials for finite temperature modelling of molecular crystals. *Chemical Science* **16**, 11419–11433. ISSN: 2041-6539. <http://dx.doi.org/10.1039/D5SC01325A> (2025).

80. Radova, M., Stark, W. G., Allen, C. S., Maurer, R. J. & Bartók, A. P. Fine-tuning foundation models of materials interatomic potentials with frozen transfer learning. *npj Computational Materials* **11**, 237. ISSN: 2057-3960. <http://dx.doi.org/10.1038/s41524-025-01727-x> (2025).
81. Liu, X. *et al.* *Fine-Tuning Universal Machine-Learned Interatomic Potentials: A Tutorial on Methods and Applications* 2025. arXiv: 2506.21935 [physics.comp-ph]. <https://arxiv.org/abs/2506.21935>.
82. Ramakrishnan, R., Dral, P. O., Rupp, M. & von Lilienfeld, O. A. Big Data Meets Quantum Chemistry Approximations: The Δ -Machine Learning Approach. *Journal of Chemical Theory and Computation* **11**, 2087–2096. ISSN: 1549-9626. <http://dx.doi.org/10.1021/acs.jctc.5b00099> (2015).
83. Lyngby, P., Larsen, C. & Jacobsen, K. W. *Bayesian optimization of atomic structures with prior probabilities from universal interatomic potentials* 2024. arXiv: 2408.15590 [cond-mat.mtrl-sci]. <https://arxiv.org/abs/2408.15590>.
84. Pitfield, J., Verner Christansen, M.-P. & Hammer, B. Active Δ -learning with universal potentials for global structure optimization. *Physical Chemistry Chemical Physics*. ISSN: 1463-9084. <http://dx.doi.org/10.1039/D5CP04302F> (2025).

Supplementary Information for “How accurate are foundational machine learning interatomic potentials for heterogeneous catalysis?”

Luuk H. E. Kempen^{1,*}, Raffaele Cheula¹, and Mie Andersen^{1,*}

¹Center for Interstellar Catalysis, Department of Physics and Astronomy, Aarhus University, Aarhus C, Denmark

*Corresponding authors: luuk@phys.au.dk, mie@phys.au.dk

S1 Machine learning interatomic potentials

Table S1: An overview of all MLIPs evaluated in this study, organized by model family and training data set. Every bullet corresponds to an evaluated MLIP.

Model family	Variant	Training data set												
		MPTrj	MPTrj+(s)Alex	OMat24	OMat24 → MPTrj + sAlex	MatPES-PBE	OC20	OC22	OC20 + OC22	OC20 → OC22	OC25	OC20 + AQCat25	OC20 → AQCat25	OC20 → OC20 + AQCat25
Allegro	L-0.1	•			•									
AQCat	31M											•	•	
	153M											•	•	
	31M inFiLM													•
	31M in+midFiLM											•		
CHGNet		•												
DimeNet ⁺⁺										• ^e				
										• ^f				
EquiformerV2	31M	•		•	•					• ^f				
	31M DeNS	•												
	83M									• ^g				
	86M				•	•								
	86M DeNS	•												
	121M ($\lambda_E = 4$, $\lambda_F = 100$)													•
	153M				•	•					• ^f			
153M DeNS	•													
eSCN	$M = 2$, 12 layers									• ^f				
	$M = 3$, 20 layers									• ^f				
eSEN	30M	•		•	•									
	small conserving												•	
	medium direct												•	

^a No strict neighbor enforcement; ^b subsampled Alexandria; ^c full Alexandria; ^d only AIMD subset; ^e All split; ^f All+MD split; ^g 2M split; ^h extended (OC20++).

Table S1: An overview of all MLIPs evaluated in this study, organized by model family and training data set. Every bullet corresponds to an evaluated MLIP.

Model family	Variant	Training data set												
		MPTrj	MPTrj + (s)Alex	OMat24	OMat24 → MPTrj + sAlex	MatPES-PBE	OC20	OC22	OC20 + OC22	OC20 → OC22	OC25	OC20 + AQCat25	OC20 → AQCat25	OC20 → OC20 + AQCat25
GemNet	dT						• ^e	•						
	OC						• ^e	•		•				
	OC ^a								•					
GRACE	1 layer small	•		•	•									
	1 layer medium			•	•									
	1 layer large			•	•									
	2 layers small	•		•	•									
	2 layers medium			•	•									
	2 layers large			•	•									
MACE	MP-0a small	•												
	MP-0a medium	•												
	MP-0a large	•												
	MP-0b3 medium	•												
	MPA-0 medium		• ^b											
	OMAT-0 small			•										
	OMAT-0 medium			•										
	MatPES-PBE-0					•								
NequIP	L-0.1	•			•									
Orb	conservative, 20 neighbors		• ^c	• ^d										
	conservative, ∞ neighbors		• ^c	• ^d										
	direct, 20 neighbors		• ^c	• ^d										
	direct, ∞ neighbors		• ^c	• ^d										
PaiNN													• ^e	
SCN													• ^f	
SevenNet	0	•		•										
	l3i5	•												
	MF		• ^b	•										
UMA	S-1.1			•									• ^h	
	M-1.1			•	•								• ^h	

^a No strict neighbor enforcement; ^b subsampled Alexandria; ^c full Alexandria; ^d only AIMD subset; ^e All split; ^f All+MD split; ^g 2M split; ^h extended (OC20++).

S2 Model prediction performance

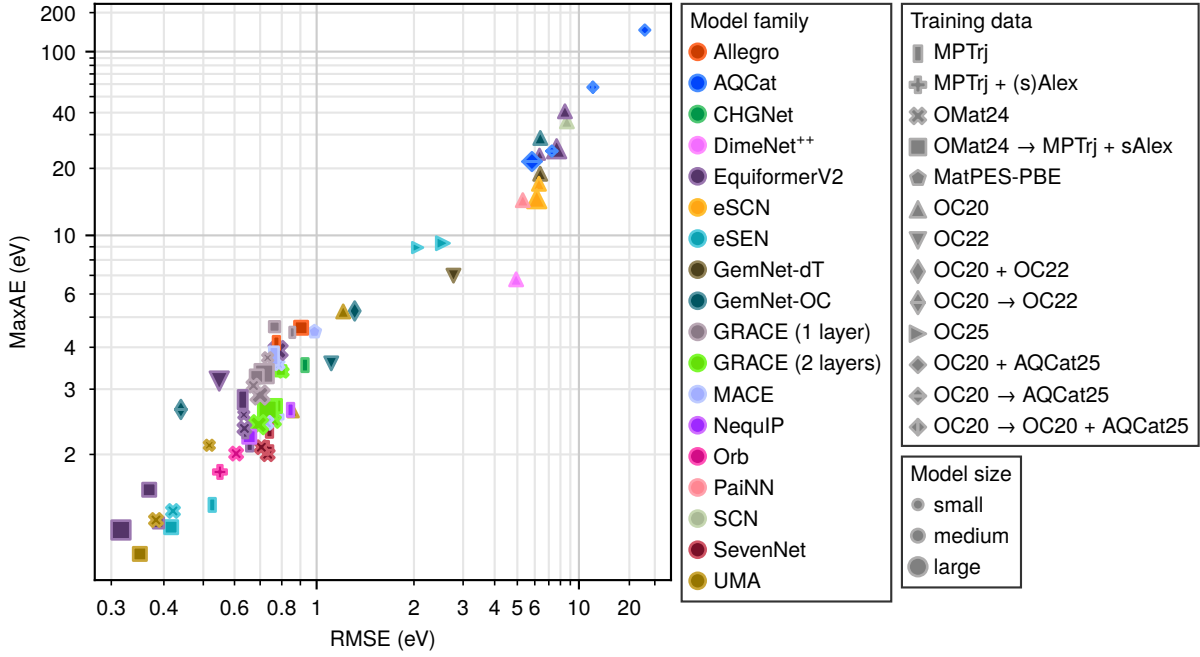


Figure S1: Prediction performance of the MLIPs for the slab vacancy formation energy of perovskite oxide surfaces.

Table S2: Prediction performance of the MLIPs for the slab vacancy formation energy of perovskite oxide surfaces.

Model family	Variant	Training data set	RMSE (eV)	MaxAE (eV)
Allegro	L-0.1	MPTrj	0.774	4.13
		OMat24 \rightarrow MPTrj + sAlex	0.904	4.62
AQCat	31M	OC20 \rightarrow AQCat25	7.25	24.5
	153M	OC20 \rightarrow AQCat25	5.82	21.6
	31M inFiLM	OC20 \rightarrow OC20 + AQCat25	12.0	57.3
	31M in+midFiLM	OC20 + AQCat25	25.4	145
CHGNet		MPTrj	0.927	3.53
DimeNet++		OC20 (All)	4.94	6.77
EquiformerV2	31M	MPTrj	0.640	2.28
		OMat24	0.634	2.54
		OMat24 \rightarrow MPTrj + sAlex	0.388	1.37
		OC20 (All+MD)	6.31	23.6
	31M DeNS	MPTrj	0.663	2.09
	83M	OC20 (2M)	8.43	40.7
	86M	OMat24	0.637	2.34
		OMat24 \rightarrow MPTrj + sAlex	0.369	1.63
	86M DeNS	MPTrj	0.657	2.12
	121M ($\lambda_E = 4, \lambda_F = 100$)	OC22	0.548	3.17
153M	OMat24	0.782	3.91	
	OMat24 \rightarrow MPTrj + sAlex	0.316	1.31	
	OC20 (All+MD)	7.65	25.2	
	MPTrj	0.630	2.80	
eSCN	$M = 2, 12$ layers	OC20 (All+MD)	6.28	16.9
	$M = 3, 20$ layers	OC20 (All+MD)	6.13	14.4
eSEN	30M	MPTrj	0.526	1.50
		OMat24	0.421	1.46
		OMat24 \rightarrow MPTrj + sAlex	0.417	1.33
	small conserving	OC25	2.06	8.93
	medium direct	OC25	2.52	9.30

^a No strict neighbor enforcement.

Table S2: Prediction performance of the MLIPs for the slab vacancy formation energy of perovskite oxide surfaces.

Model family	Variant	Training data set	RMSE (eV)	MaxAE (eV)
GemNet	dT	OC20 (All)	6.36	18.8
		OC22	2.76	6.98
	OC	OC20 (All)	6.37	28.8
		OC22	1.10	3.57
		OC20 + OC22	1.29	5.25
		OC20 \rightarrow OC22	0.440	2.63
OC ^a	OC20 + OC22	1.29	5.24	
GRACE	1 layer small	MPTrj	0.855	4.46
		OMat24	0.733	3.71
	1 layer medium	OMat24 \rightarrow MPTrj + sAlex	0.765	4.65
		OMat24	0.672	3.07
	1 layer large	OMat24 \rightarrow MPTrj + sAlex	0.686	3.27
		OMat24	0.700	2.89
	2 layers small	OMat24 \rightarrow MPTrj + sAlex	0.717	3.33
		MPTrj	0.787	3.89
	2 layers medium	OMat24	0.806	3.37
		OMat24 \rightarrow MPTrj + sAlex	0.795	3.39
	2 layers large	OMat24	0.762	2.45
		OMat24 \rightarrow MPTrj + sAlex	0.767	2.69
MACE	MP-0a small	MPTrj	0.853	3.54
	MP-0a medium	MPTrj	0.909	4.21
	MP-0a large	MPTrj	0.762	3.76
	MP-0b3 medium	MPTrj	0.866	4.03
	MPA-0 medium	MPTrj + sAlex	0.774	2.51
	OMAT-0 small	OMat24	0.786	3.54
	OMAT-0 medium	OMat24	0.727	2.42
	MatPES-PBE-0	MatPES-PBE	0.986	4.48
NequIP	L-0.1	MPTrj	0.845	2.62
		OMat24 \rightarrow MPTrj + sAlex	0.655	2.22
Orb	conservative, 20 neighbors	MPTrj + Alex	0.588	1.76
		OMat24 (only AIMD)	0.606	2.01
	conservative, ∞ neighbors	MPTrj + Alex	0.551	1.81
		OMat24 (only AIMD)	0.613	1.73
	direct, 20 neighbors	MPTrj + Alex	0.752	2.71
		OMat24 (only AIMD)	0.682	2.55
direct, ∞ neighbors	MPTrj + Alex	0.783	3.08	
	OMat24 (only AIMD)	0.670	2.94	
PaiNN		OC20 (All)	5.29	14.2
SCN		OC20 (All+MD)	8.63	35.6
SevenNet	0	MPTrj	0.868	3.08
		OMat24	0.705	2.09
	13i5	MPTrj	0.741	2.30
		OMat24	0.733	2.00
MF	MPTrj + sAlex	0.727	2.08	
	OC20++	0.860	2.59	
UMA	S-1.1	OMat24	0.518	2.11
		OC20++	1.19	5.23
	M-1.1	OMat24	0.383	1.39
		OMat24 \rightarrow MPTrj + sAlex	0.350	1.16

^a No strict neighbor enforcement.

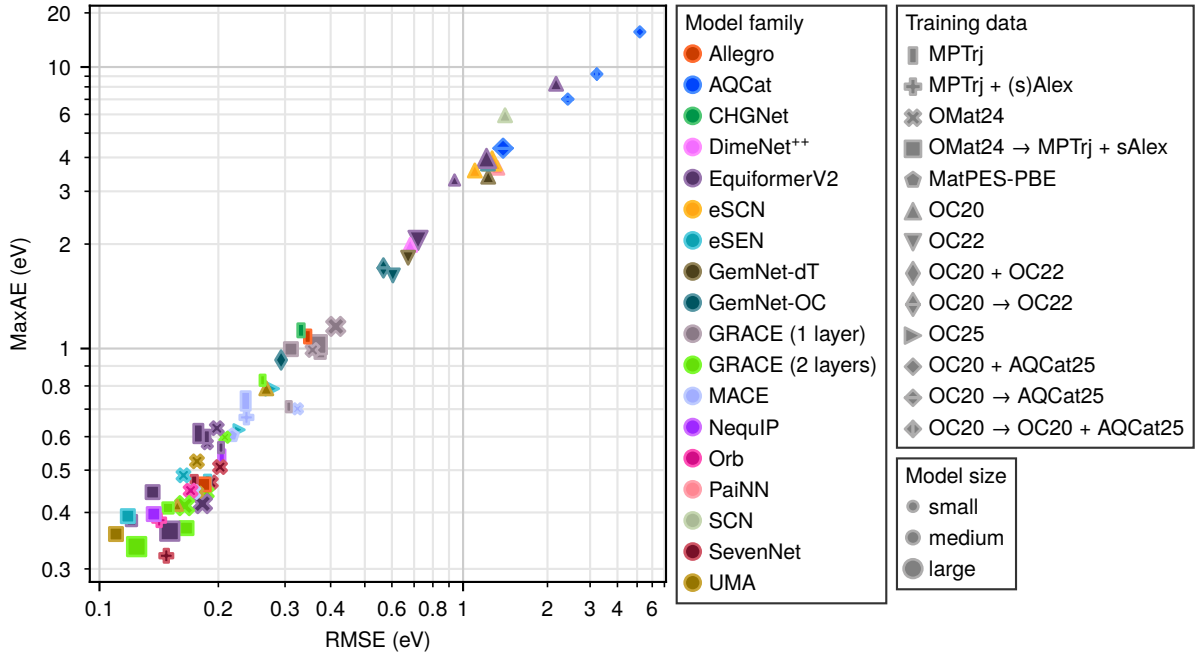


Figure S2: Prediction performance of the MLIPs for the activation energy of CO_2 hydrogenation reaction steps on (doped) $\text{ZrO}_2(101)$ surfaces.

Table S3: Prediction performance of the MLIPs for the activation energy of (doped) $\text{ZrO}_2(101)$ surfaces.

Model family	Variant	Training data set	RMSE (eV)	MaxAE (eV)	
Allegro	L-0.1	MPTrj	0.346	1.08	
		OMat24 \rightarrow MPTrj + sAlex	0.183	0.463	
AQCat	31M	OC20 \rightarrow AQCat25	2.41	7.02	
		153M	OC20 \rightarrow AQCat25	1.37	4.35
		31M inFiLM	OC20 \rightarrow OC20 + AQCat25	3.21	9.22
		31M in+midFiLM	OC20 + AQCat25	5.16	15.4
CHGNet		MPTrj	0.331	1.12	
DimeNet ⁺⁺		OC20 (All)	0.681	1.99	
EquiformerV2	31M	MPTrj	0.216	0.560	
		OMat24	0.187	0.577	
		OMat24 \rightarrow MPTrj + sAlex	0.120	0.384	
		OC20 (All+MD)	0.938	3.29	
	31M DeNS	MPTrj	0.203	0.565	
		83M	OC20 (2M)	2.16	8.28
	86M	OMat24	0.198	0.629	
		OMat24 \rightarrow MPTrj + sAlex	0.136	0.445	
		86M DeNS	MPTrj	0.187	0.600
		121M ($\lambda_E = 4, \lambda_F = 100$)	OC22	0.720	2.05
153M	OMat24	0.182	0.419		
	OMat24 \rightarrow MPTrj + sAlex	0.150	0.363		
	OC20 (All+MD)	1.20	3.97		
	MPTrj	0.178	0.611		
eSCN	153M DeNS	OC20 (All+MD)	1.09	3.57	
		$M = 2, 12$ layers	1.25	3.88	
		$M = 3, 20$ layers	1.25	3.88	
eSEN	30M	MPTrj	0.188	0.470	
		OMat24	0.163	0.486	
		OMat24 \rightarrow MPTrj + sAlex	0.118	0.392	
	small conserving	OC25	0.227	0.623	
	medium direct	OC25	0.277	0.787	

^a No strict neighbor enforcement.

Table S3: Prediction performance of the MLIPs for the activation energy of (doped) $\text{ZrO}_2(101)$ surfaces.

Model family	Variant	Training data set	RMSE (eV)	MaxAE (eV)
GemNet	dT	OC20 (All)	1.21	3.39
		OC22	0.671	1.81
	OC	OC20 (All)	1.21	3.79
		OC22	0.604	1.60
		OC20 + OC22	0.293	0.933
		OC20 \rightarrow OC22	0.566	1.69
OC ^a	OC20 + OC22	0.293	0.933	
GRACE	1 layer small	MPTrj	0.307	0.710
		OMat24	0.376	1.03
		OMat24 \rightarrow MPTrj + sAlex	0.374	0.972
	1 layer medium	OMat24	0.356	0.991
		OMat24 \rightarrow MPTrj + sAlex	0.311	0.996
	1 layer large	OMat24	0.413	1.15
		OMat24 \rightarrow MPTrj + sAlex	0.367	1.02
	2 layers small	MPTrj	0.261	0.827
		OMat24	0.208	0.598
		OMat24 \rightarrow MPTrj + sAlex	0.149	0.409
	2 layers medium	OMat24	0.187	0.443
		OMat24 \rightarrow MPTrj + sAlex	0.166	0.369
2 layers large	OMat24	0.164	0.414	
	OMat24 \rightarrow MPTrj + sAlex	0.124	0.336	
MACE	MP-0a small	MPTrj	0.257	0.935
	MP-0a medium	MPTrj	0.300	1.00
	MP-0a large	MPTrj	0.236	0.734
	MP-0b3 medium	MPTrj	0.404	1.01
	MPA-0 medium	MPTrj + sAlex	0.237	0.668
	OMAT-0 small	OMat24	0.324	0.701
	OMAT-0 medium	OMat24	0.172	0.445
	MatPES-PBE-0	MatPES-PBE	0.217	0.604
NequIP	L-0.1	MPTrj	0.204	0.539
		OMat24 \rightarrow MPTrj + sAlex	0.137	0.397
Orb	conservative, 20 neighbors	MPTrj + Alex	0.154	0.414
		OMat24 (only AIMD)	0.181	0.485
	conservative, ∞ neighbors	MPTrj + Alex	0.141	0.384
		OMat24 (only AIMD)	0.170	0.449
	direct, 20 neighbors	MPTrj + Alex	0.161	0.392
		OMat24 (only AIMD)	0.196	0.591
	direct, ∞ neighbors	MPTrj + Alex	0.203	0.588
		OMat24 (only AIMD)	0.235	0.682
PaiNN		OC20 (All)	1.31	3.66
SCN		OC20 (All+MD)	1.39	5.95
SevenNet	0	MPTrj	0.173	0.470
		OMat24	0.202	0.508
	13i5	MPTrj	0.188	0.438
		OMat24	0.191	0.468
	MF	MPTrj + sAlex	0.147	0.321
UMA	S-1.1	OC20++	0.157	0.415
		OMat24	0.177	0.445
	M-1.1	OC20++	0.267	0.789
		OMat24 \rightarrow MPTrj + sAlex	0.110	0.358

^a No strict neighbor enforcement.

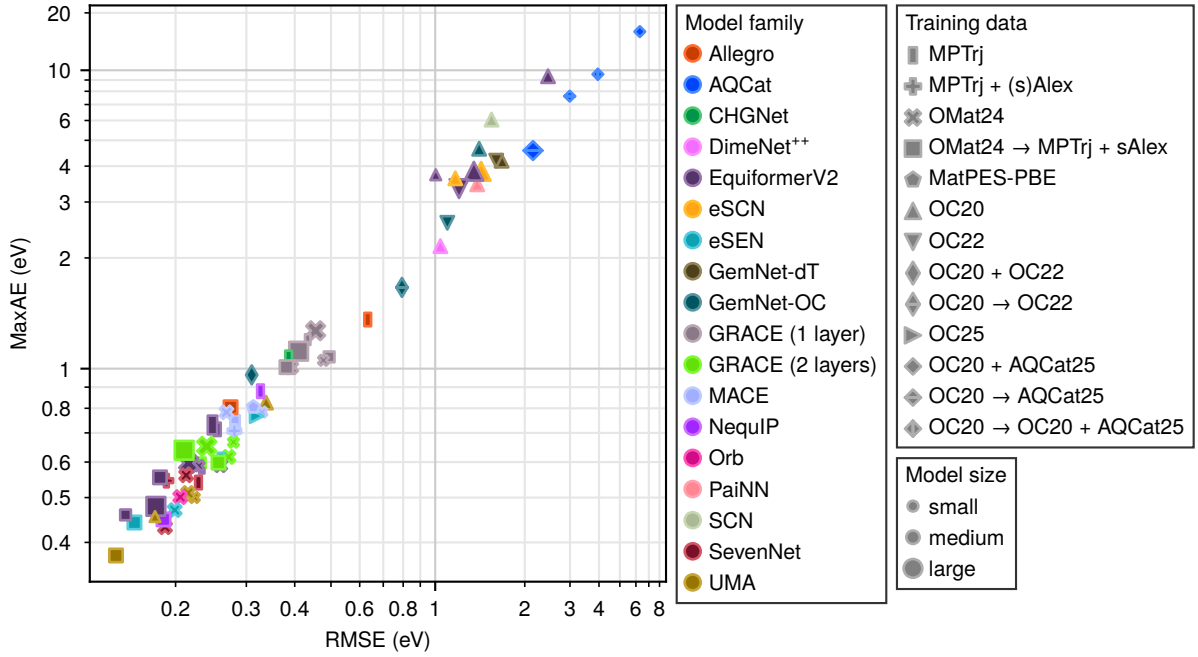


Figure S3: Prediction performance of the MLIPs for the reaction energy of CO_2 hydrogenation reaction steps on (doped) $\text{ZrO}_2(101)$ surfaces.

Table S4: Prediction performance of the MLIPs for the reaction energy of (doped) $\text{ZrO}_2(101)$ surfaces.

Model family	Variant	Training data set	RMSE (eV)	MaxAE (eV)
Allegro	L-0.1	MPTrj	0.632	1.34
		OMat24 \rightarrow MPTrj + sAlex	0.274	0.805
AQCat	31M	OC20 \rightarrow AQCat25	2.99	7.61
	153M	OC20 \rightarrow AQCat25	2.15	4.57
	31M inFiLM	OC20 \rightarrow OC20 + AQCat25	3.95	9.57
	31M in+midFiLM	OC20 + AQCat25	6.28	15.7
CHGNet		MPTrj	0.386	1.07
DimeNet ⁺⁺		OC20 (All)	1.04	2.17
EquiformerV2	31M	MPTrj	0.250	0.535
		OMat24	0.228	0.589
		OMat24 \rightarrow MPTrj + sAlex	0.151	0.458
	31M DeNS	OC20 (All+MD)	1.00	3.72
		MPTrj	0.232	0.581
	83M	OC20 (2M)	2.45	9.37
EquiformerV2	86M	OMat24	0.258	0.590
		OMat24 \rightarrow MPTrj + sAlex	0.183	0.554
	86M DeNS	MPTrj	0.254	0.713
	121M ($\lambda_E = 4, \lambda_F = 100$)	OC22	1.19	3.33
EquiformerV2	153M	OMat24	0.215	0.597
		OMat24 \rightarrow MPTrj + sAlex	0.179	0.478
	153M DeNS	OC20 (All+MD)	1.33	3.83
		MPTrj	0.247	0.730
eSCN	$M = 2, 12$ layers	OC20 (All+MD)	1.16	3.62
	$M = 3, 20$ layers	OC20 (All+MD)	1.41	3.83
		MPTrj	0.259	0.608
eSEN	30M	OMat24	0.199	0.469
		OMat24 \rightarrow MPTrj + sAlex	0.159	0.441
		MPTrj	0.259	0.608
	small conserving	OC25	0.256	0.600
medium direct	OC25	0.319	0.766	

^a No strict neighbor enforcement.

Table S4: Prediction performance of the MLIPs for the reaction energy of (doped) ZrO₂(101) surfaces.

Model family	Variant	Training data set	RMSE (eV)	MaxAE (eV)
GemNet	dT	OC20 (All)	1.65	4.19
		OC22	1.58	4.19
	OC	OC20 (All)	1.38	4.64
		OC22	1.09	2.57
		OC20 + OC22	0.310	0.965
		OC20 → OC22	0.794	1.64
OC ^a	OC20 + OC22	0.310	0.965	
GRACE	1 layer small	MPTrj	0.433	1.19
		OMat24	0.477	1.05
		OMat24 → MPTrj + sAlex	0.494	1.07
	1 layer medium	OMat24	0.392	1.01
		OMat24 → MPTrj + sAlex	0.381	1.01
	1 layer large	OMat24	0.454	1.25
		OMat24 → MPTrj + sAlex	0.410	1.11
	2 layers small	MPTrj	0.416	1.13
		OMat24	0.278	0.666
		OMat24 → MPTrj + sAlex	0.230	0.597
	2 layers medium	OMat24	0.270	0.616
		OMat24 → MPTrj + sAlex	0.255	0.598
	2 layers large	OMat24	0.239	0.652
		OMat24 → MPTrj + sAlex	0.210	0.638
MACE	MP-0a small	MPTrj	0.422	0.947
	MP-0a medium	MPTrj	0.482	1.16
	MP-0a large	MPTrj	0.281	0.732
	MP-0b3 medium	MPTrj	0.563	1.42
	MPA-0 medium	MPTrj + sAlex	0.280	0.707
	OMAT-0 small	OMat24	0.329	0.784
	OMAT-0 medium	OMat24	0.267	0.783
	MatPES-PBE-0	MatPES-PBE	0.312	0.805
NequIP	L-0.1	MPTrj	0.326	0.880
		OMat24 → MPTrj + sAlex	0.187	0.448
Orb	conservative, 20 neighbors	MPTrj + Alex	0.184	0.422
		OMat24 (only AIMD)	0.205	0.501
	conservative, ∞ neighbors	MPTrj + Alex	0.181	0.480
		OMat24 (only AIMD)	0.208	0.517
	direct, 20 neighbors	MPTrj + Alex	0.202	0.453
		OMat24 (only AIMD)	0.254	0.603
	direct, ∞ neighbors	MPTrj + Alex	0.234	0.561
		OMat24 (only AIMD)	0.265	0.509
PaiNN		OC20 (All)	1.36	3.45
SCN		OC20 (All+MD)	1.52	6.05
SevenNet	0	MPTrj	0.228	0.540
		OMat24	0.188	0.431
	13i5	MPTrj	0.275	0.704
		OMat24	0.212	0.560
	MF	MPTrj + sAlex	0.190	0.545
UMA	S-1.1	OC20++	0.178	0.455
		OMat24	0.222	0.500
	M-1.1	OC20++	0.337	0.826
		OMat24	0.215	0.512
		OMat24 → MPTrj + sAlex	0.144	0.375

^a No strict neighbor enforcement.

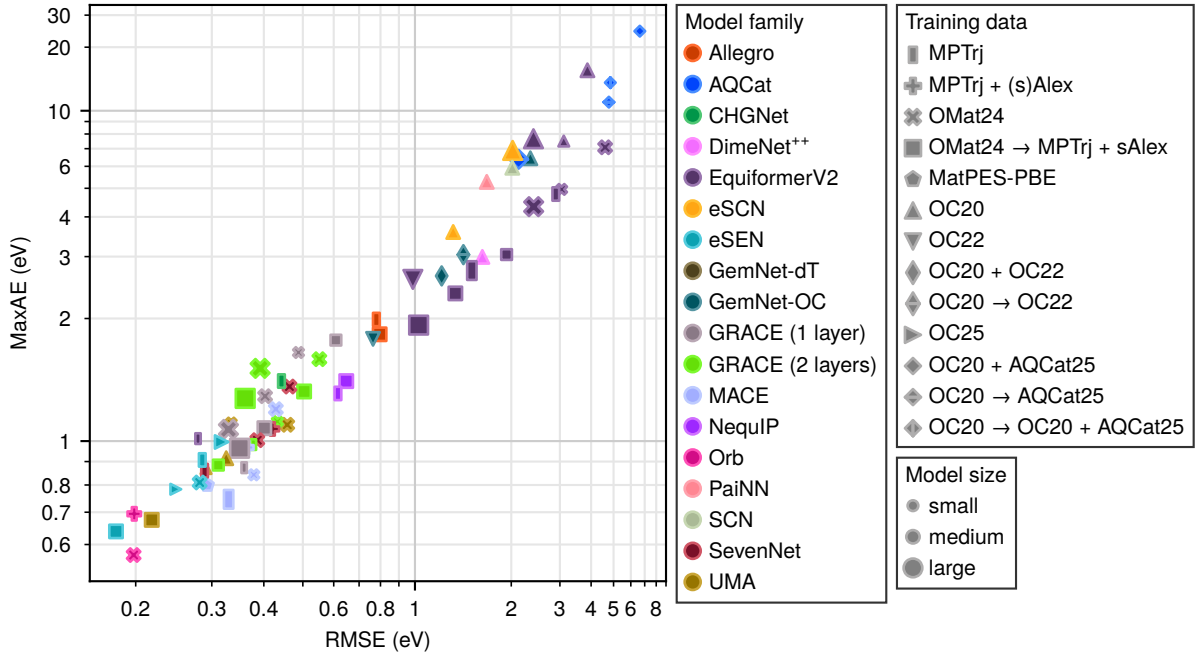


Figure S4: Prediction performance of the MLIPs for the formation energy of adsorbates of CO_2 hydrogenation reaction steps on (doped) $\text{ZrO}_2(101)$ surfaces.

Table S5: Prediction performance of the MLIPs for the formation energy of adsorbates of (doped) $\text{ZrO}_2(101)$ surfaces.

Model family	Variant	Training data set	RMSE (eV)	MaxAE (eV)	
Allegro	L-0.1	MPTrj	0.779	1.99	
		OMat24 \rightarrow MPTrj + sAlex	0.796	1.82	
AQCat	31M	OC20 \rightarrow AQCat25	4.77	10.9	
		153M	OC20 \rightarrow AQCat25	2.12	6.38
		31M inFiLM	OC20 \rightarrow OC20 + AQCat25	4.84	13.4
		31M in+midFiLM	OC20 + AQCat25	6.63	24.4
CHGNet		MPTrj	0.442	1.38	
DimeNet ⁺⁺	31M	OC20 (All)	1.60	2.99	
		MPTrj	0.278	1.01	
EquiformerV2	31M	OMat24	3.05	4.96	
		OMat24 \rightarrow MPTrj + sAlex	1.93	3.04	
		OC20 (All+MD)	3.10	7.50	
		MPTrj	1.19	2.42	
	31M DeNS	OC20 (2M)	3.86	15.3	
	83M	OMat24	4.59	7.09	
	86M	OMat24 \rightarrow MPTrj + sAlex	1.32	2.34	
		MPTrj	2.89	4.78	
	121M ($\lambda_E = 4, \lambda_F = 100$)	OC22	0.986	2.57	
	153M	OMat24	2.40	4.32	
OMat24 \rightarrow MPTrj + sAlex		1.02	1.92		
OC20 (All+MD)		2.39	7.66		
MPTrj		1.48	2.73		
eSCN	153M DeNS	MPTrj	1.48	2.73	
	$M = 2, 12$ layers	OC20 (All+MD)	1.30	3.57	
	$M = 3, 20$ layers	OC20 (All+MD)	2.02	6.89	
eSEN	30M	MPTrj	0.285	0.907	
		OMat24	0.281	0.810	
		OMat24 \rightarrow MPTrj + sAlex	0.180	0.638	
	small conserving	OC25	0.247	0.783	
	medium direct	OC25	0.316	0.995	

^a No strict neighbor enforcement.

Table S5: Prediction performance of the MLIPs for the formation energy of adsorbates of (doped) $\text{ZrO}_2(101)$ surfaces.

Model family	Variant	Training data set	RMSE (eV)	MaxAE (eV)	
GemNet	dT	OC20 (All)	–	–	
		OC22	–	–	
	OC	OC20 (All)	2.33	6.43	
		OC22	0.763	1.77	
		OC20 + OC22	1.20	2.63	
OC ^a	OC20 → OC22	1.40	3.04		
	OC20 + OC22	1.20	2.63		
GRACE	1 layer small	MPTrj	0.358	0.872	
		OMat24	0.488	1.63	
	1 layer medium	OMat24 → MPTrj + sAlex	0.608	1.75	
		OMat24	0.403	1.27	
	1 layer large	OMat24 → MPTrj + sAlex	0.401	1.07	
		OMat24	0.329	1.06	
	2 layers small	OMat24 → MPTrj + sAlex	0.349	0.964	
		MPTrj	0.377	0.982	
	2 layers medium	OMat24	0.432	1.11	
		OMat24 → MPTrj + sAlex	0.311	0.884	
	2 layers large	OMat24	0.551	1.57	
		OMat24 → MPTrj + sAlex	0.504	1.31	
	MACE	MP-0a small	MPTrj	0.360	0.912
		MP-0a medium	MPTrj	0.512	1.07
MP-0a large		MPTrj	0.329	0.745	
MP-0b3 medium		MPTrj	0.451	1.50	
MPA-0 medium		MPTrj + sAlex	0.364	0.968	
OMAT-0 small		OMat24	0.378	0.842	
OMAT-0 medium		OMat24	0.428	1.18	
MatPES-PBE-0		MatPES-PBE	0.293	0.799	
NequIP	L-0.1	MPTrj	0.615	1.29	
		OMat24 → MPTrj + sAlex	0.647	1.38	
Orb	conservative, 20 neighbors	MPTrj + Alex	0.198	0.695	
		OMat24 (only AIMD)	0.198	0.571	
	conservative, ∞ neighbors	MPTrj + Alex	0.241	0.812	
		OMat24 (only AIMD)	0.243	0.838	
	direct, 20 neighbors	MPTrj + Alex	0.311	0.761	
		OMat24 (only AIMD)	0.310	0.698	
	direct, ∞ neighbors	MPTrj + Alex	0.286	0.901	
		OMat24 (only AIMD)	0.329	1.08	
PaiNN		OC20 (All)	1.66	5.27	
SCN		OC20 (All+MD)	2.02	5.93	
SevenNet	0	MPTrj	0.288	0.859	
		OMat24	0.386	1.00	
	13i5	MPTrj	0.350	1.01	
		OMat24	0.463	1.34	
MF	MPTrj + sAlex	0.420	1.07		
	OC20++	0.291	0.869		
UMA	S-1.1	OMat24	0.333	1.10	
		OC20++	0.325	0.916	
	M-1.1	OMat24	0.457	1.09	
		OMat24 → MPTrj + sAlex	0.218	0.675	

^a No strict neighbor enforcement.

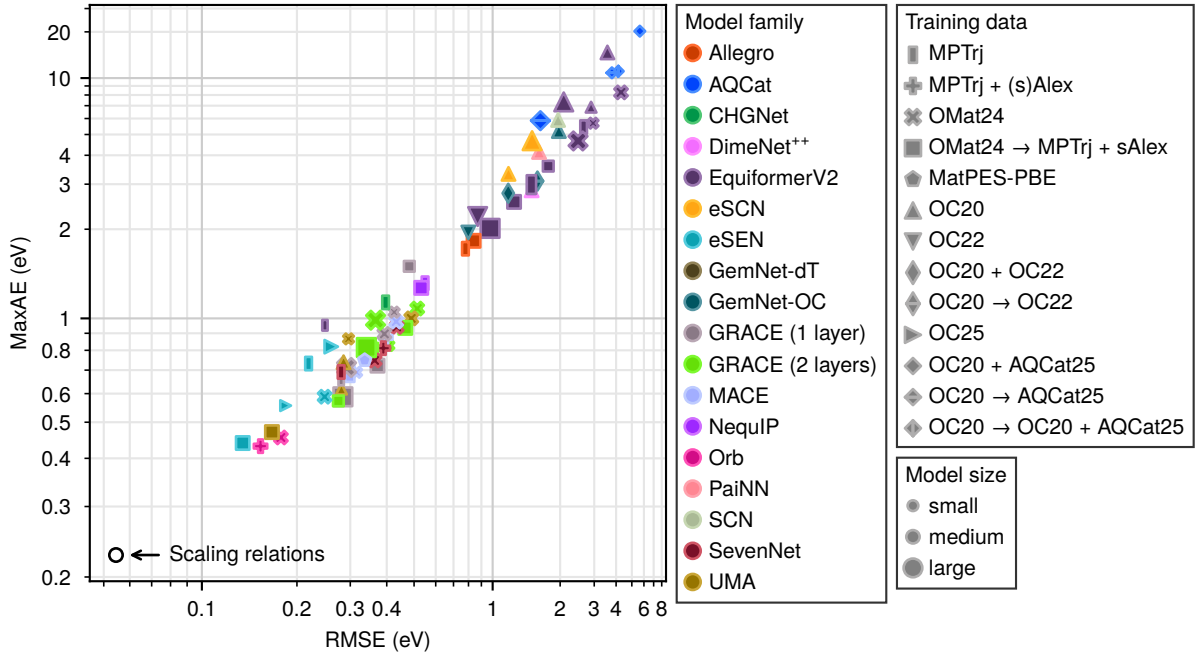


Figure S5: Prediction performance of the MLIPs for the formation energy of TSs of CO_2 hydrogenation reaction steps on (doped) $\text{ZrO}_2(101)$ surfaces.

Table S6: Prediction performance of the MLIPs for the formation energy of TSs of (doped) $\text{ZrO}_2(101)$ surfaces.

Model family	Variant	Training data set	RMSE (eV)	MaxAE (eV)	
Allegro	L-0.1	MPTrj	0.778	1.70	
		OMat24 \rightarrow MPTrj + sAlex	0.838	1.81	
AQCat	31M	OC20 \rightarrow AQCat25	3.78	10.8	
		153M	OC20 \rightarrow AQCat25	1.61	5.85
		31M inFiLM	OC20 \rightarrow OC20 + AQCat25	4.12	11.0
		31M in+midFiLM	OC20 + AQCat25	5.63	20.2
CHGNet		MPTrj	0.396	1.12	
DimeNet ⁺⁺	31M	OC20 (All)	1.47	2.83	
		MPTrj	0.247	0.952	
EquiformerV2	31M	OMat24	2.96	5.68	
		OMat24 \rightarrow MPTrj + sAlex	1.75	3.58	
		OC20 (All+MD)	2.88	6.87	
		MPTrj	1.19	2.59	
	31M DeNS	OC20 (2M)	3.56	14.4	
	83M	OMat24	4.28	8.27	
	86M	OMat24 \rightarrow MPTrj + sAlex	1.23	2.54	
		MPTrj	2.63	5.44	
	121M ($\lambda_E = 4, \lambda_F = 100$)	OC22	0.869	2.23	
	153M	OMat24	2.46	4.66	
OMat24 \rightarrow MPTrj + sAlex		0.976	2.01		
OC20 (All+MD)		2.08	7.34		
MPTrj		1.47	2.99		
eSCN	153M DeNS	MPTrj	1.47	2.99	
	$M = 2, 12$ layers	OC20 (All+MD)	1.16	3.32	
	$M = 3, 20$ layers	OC20 (All+MD)	1.48	4.67	
eSEN	30M	MPTrj	0.218	0.731	
		OMat24	0.246	0.588	
		OMat24 \rightarrow MPTrj + sAlex	0.134	0.439	
	small conserving	OC25	0.184	0.555	
	medium direct	OC25	0.259	0.820	

^a No strict neighbor enforcement.

Table S6: Prediction performance of the MLIPs for the formation energy of TSs of (doped) $\text{ZrO}_2(101)$ surfaces.

Model family	Variant	Training data set	RMSE (eV)	MaxAE (eV)	
GemNet	dT	OC20 (All)	–	–	
		OC22	–	–	
	OC	OC20 (All)	1.97	5.20	
		OC22	0.799	1.94	
		OC20 + OC22	1.16	2.75	
GRACE	OC ^a	OC20 → OC22	1.56	3.09	
		OC20 + OC22	1.16	2.75	
	1 layer small	MPTrj	0.280	0.656	
		OMat24	0.425	1.05	
		OMat24 → MPTrj + sAlex	0.481	1.48	
	1 layer medium	OMat24	0.392	0.896	
		OMat24 → MPTrj + sAlex	0.371	0.721	
	1 layer large	OMat24	0.291	0.712	
		OMat24 → MPTrj + sAlex	0.283	0.588	
	2 layers small	MPTrj	0.365	0.812	
OMat24		0.407	0.827		
OMat24 → MPTrj + sAlex		0.274	0.573		
2 layers medium		OMat24	0.513	1.07	
2 layers medium	OMat24 → MPTrj + sAlex	0.465	0.935		
	2 layers large	OMat24	0.366	0.987	
MACE	MP-0a small	OMat24 → MPTrj + sAlex	0.340	0.815	
		MPTrj	0.412	0.845	
	MP-0a medium	MPTrj	0.471	0.874	
	MP-0a large	MPTrj	0.299	0.689	
	MP-0b3 medium	MPTrj	0.528	1.27	
	MPA-0 medium	MPTrj + sAlex	0.397	0.875	
	OMAT-0 small	OMat24	0.315	0.690	
	OMAT-0 medium	OMat24	0.432	0.977	
MatPES-PBE-0	MatPES-PBE	0.336	0.748		
	NequIP	L-0.1	MPTrj	0.548	1.30
Orb	conservative, 20 neighbors	OMat24 → MPTrj + sAlex	0.531	1.25	
		MPTrj + Alex	0.153	0.431	
	conservative, ∞ neighbors	OMat24 (only AIMD)	0.178	0.455	
		MPTrj + Alex	0.198	0.639	
	direct, 20 neighbors	OMat24 (only AIMD)	0.212	0.606	
		MPTrj + Alex	0.260	0.631	
	direct, ∞ neighbors	OMat24 (only AIMD)	0.285	0.577	
		MPTrj + Alex	0.226	0.546	
	PaiNN	SCN	OMat24 (only AIMD)	0.278	0.753
			OC20 (All)	1.59	4.14
SevenNet	0	OC20 (All+MD)	1.95	5.90	
		MPTrj	0.279	0.691	
	13i5	OMat24	0.363	0.747	
		MPTrj	0.318	0.824	
	MF	OMat24	0.434	0.941	
MPTrj + sAlex		0.389	0.812		
UMA	S-1.1	OC20++	0.280	0.618	
		OMat24	0.296	0.866	
	M-1.1	OC20++	0.285	0.738	
		OMat24	0.489	1.00	
		OMat24 → MPTrj + sAlex	0.166	0.470	
Scaling relations [1]			0.0545	0.227	

^a No strict neighbor enforcement.

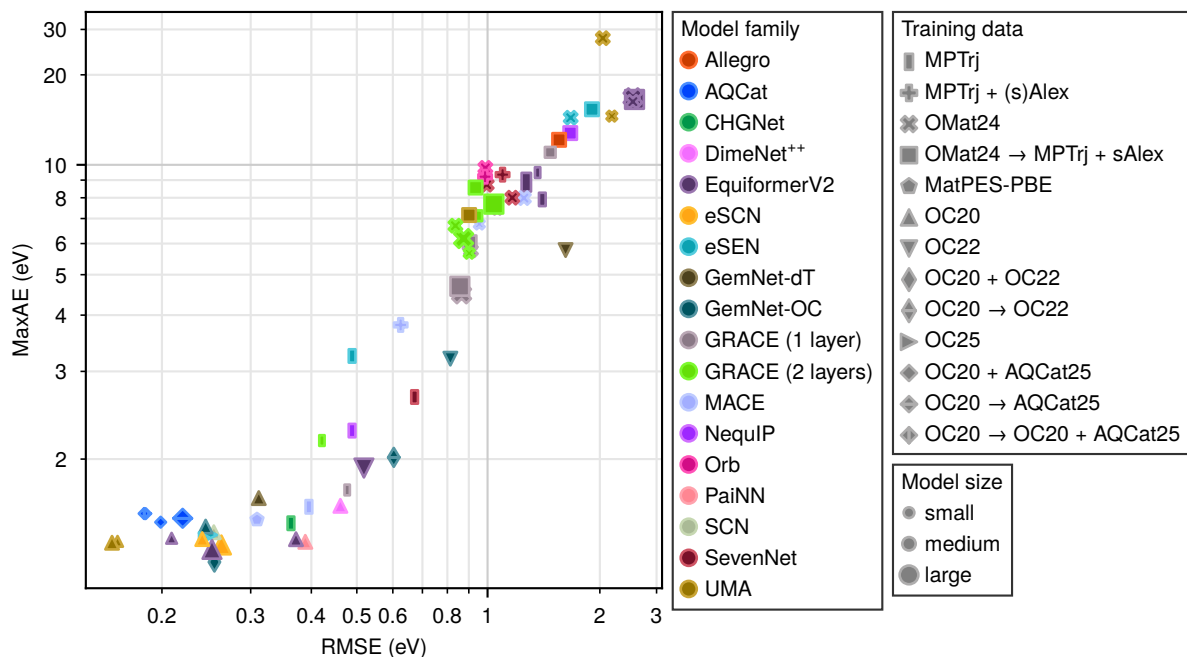


Figure S6: Prediction performance of the MLIPs for the activation energy of RWGS reaction steps on metals and SAAs.

Table S7: Prediction performance of the MLIPs for the activation energy of RWGS reaction steps on metals and SAAs.

Model family	Variant	Training data set	RMSE (eV)	MaxAE (eV)
Allegro	L-0.1	MPTrj	0.882	4.73
		OMat24 \rightarrow MPTrj + sAlex	1.53	12.0
AQCat	{ 31M 153M 31M inFiLM 31M in+midFiLM	OC20 \rightarrow AQCat25	0.186	1.59
		OC20 \rightarrow AQCat25	0.220	1.56
		OC20 \rightarrow OC20 + AQCat25	0.185	1.59
		OC20 + AQCat25	0.199	1.53
CHGNet		MPTrj	0.363	1.53
DimeNet ⁺⁺		OC20 (All)	0.461	1.64
EquiformerV2	31M	MPTrj	1.34	9.48
		OMat24	2.54	16.1
		OMat24 \rightarrow MPTrj + sAlex	2.57	16.1
		OC20 (All+MD)	0.209	1.44
	31M DeNS	MPTrj	1.38	7.96
		OC20 (2M)	0.372	1.43
	86M	OMat24	2.52	16.0
		OMat24 \rightarrow MPTrj + sAlex	2.57	16.0
		MPTrj	1.38	7.91
		121M ($\lambda_E = 4, \lambda_F = 100$)	OC22	0.518
153M	OMat24	2.52	16.5	
	OMat24 \rightarrow MPTrj + sAlex	2.55	16.3	
	OC20 (All+MD)	0.251	1.37	
	MPTrj	1.25	8.87	
eSCN	{ $M = 2, 12$ layers $M = 3, 20$ layers	OC20 (All+MD)	0.240	1.43
		OC20 (All+MD)	0.262	1.40
		MPTrj	0.488	3.24
eSEN	30M	OMat24	1.65	14.1
		OMat24 \rightarrow MPTrj + sAlex	1.90	15.1
		OC25	0.242	1.44
	small conserving	OC25	0.249	1.46
	medium direct	OC25	0.249	1.46

^a No strict neighbor enforcement.

Table S7: Prediction performance of the MLIPs for the activation energy of RWGS reaction steps on metals and SAAs.

Model family	Variant	Training data set	RMSE (eV)	MaxAE (eV)
GemNet	dT	OC20 (All)	0.312	1.69
		OC22	1.60	5.77
	OC	OC20 (All)	0.244	1.51
		OC22	0.813	3.19
		OC20 + OC22	0.254	1.31
GRACE	OC ^a	OC20 → OC22	0.603	2.02
	1 layer small	OC20 + OC22	0.254	1.31
		MPTrj	0.477	1.75
		OMat24	1.06	7.43
	1 layer medium	OMat24 → MPTrj + sAlex	1.45	10.9
		OMat24	0.911	5.76
	1 layer large	OMat24 → MPTrj + sAlex	0.904	6.05
		OMat24	0.865	4.49
	2 layers small	OMat24 → MPTrj + sAlex	0.856	4.68
		MPTrj	0.421	2.17
		OMat24	0.902	5.66
2 layers medium	OMat24 → MPTrj + sAlex	0.941	7.12	
	OMat24	0.836	6.69	
	OMat24 → MPTrj + sAlex	0.935	8.56	
2 layers large	OMat24	0.874	6.18	
	OMat24 → MPTrj + sAlex	1.04	7.67	
	MP-0a small	MPTrj	0.625	2.93
MACE	MP-0a medium	MPTrj	0.574	2.39
	MP-0a large	MPTrj	0.601	3.23
	MP-0b3 medium	MPTrj	0.395	1.63
	MPA-0 medium	MPTrj + sAlex	0.625	3.80
	OMAT-0 small	OMat24	0.954	6.76
	OMAT-0 medium	OMat24	1.24	7.98
	MatPES-PBE-0	MatPES-PBE	0.309	1.55
	NequIP	L-0.1	MPTrj	0.488
OMat24 → MPTrj + sAlex			1.65	12.6
Orb	conservative, 20 neighbors	MPTrj + Alex	2.34	15.6
		OMat24 (only AIMD)	1.64	10.3
	conservative, ∞ neighbors	MPTrj + Alex	1.14	9.28
		OMat24 (only AIMD)	0.987	9.79
	direct, 20 neighbors	MPTrj + Alex	1.22	8.98
		OMat24 (only AIMD)	1.53	11.0
	direct, ∞ neighbors	MPTrj + Alex	0.986	9.21
PaiNN SCN		OMat24 (only AIMD)	1.05	10.1
		OC20 (All)	0.389	1.42
SevenNet	0	OC20 (All+MD)	0.253	1.47
		MPTrj	0.717	3.51
	13i5	OMat24	1.15	8.00
		MPTrj	0.672	2.65
	MF	OMat24	0.995	8.73
MPTrj + sAlex		1.09	9.34	
UMA	S-1.1	OC20++	0.164	1.42
		OMat24	2.17	14.3
	M-1.1	OC20++	0.160	1.41
		OMat24	2.04	27.7
		OMat24 → MPTrj + sAlex	0.902	7.16

^a No strict neighbor enforcement.

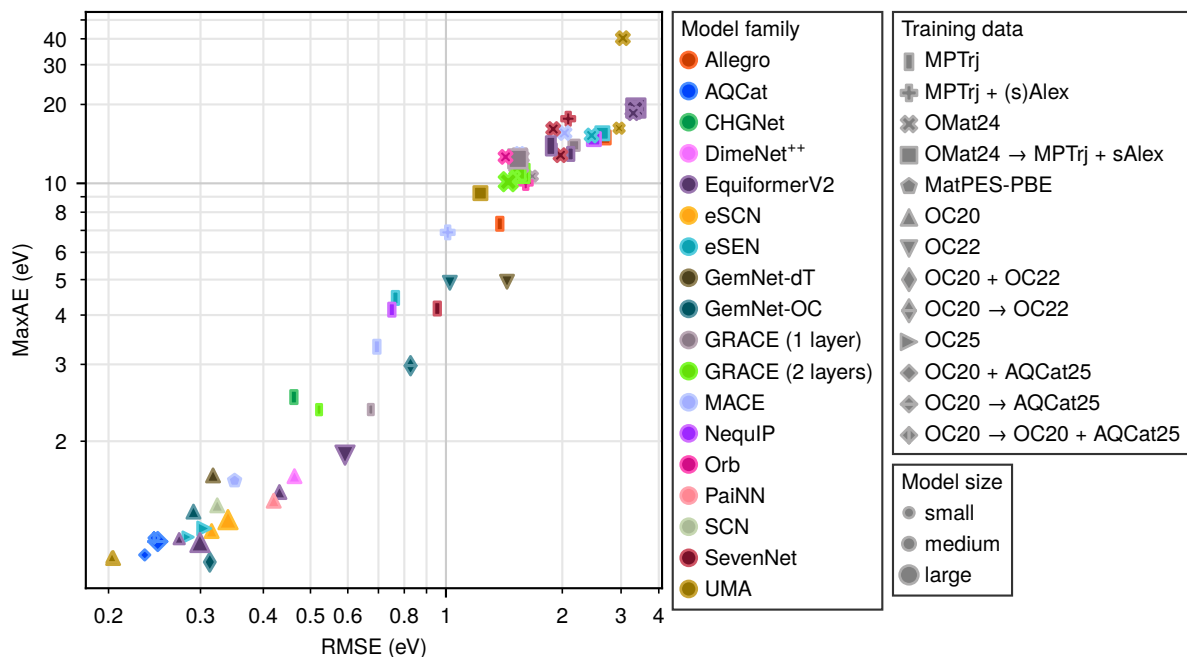


Figure S7: Prediction performance of the MLIPs for the reaction energy of RWGS reaction steps on metals and SAAs.

Table S8: Prediction performance of the MLIPs for the reaction energy of RWGS reaction steps on metals and SAAs.

Model family	Variant	Training data set	RMSE (eV)	MaxAE (eV)	
Allegro	L-0.1	MPTrj	1.36	7.34	
		OMat24 \rightarrow MPTrj + sAlex	2.65	14.7	
AQCat	31M	OC20 \rightarrow AQCat25	0.249	1.24	
		OC20 \rightarrow AQCat25	0.248	1.25	
		31M inFiLM	OC20 \rightarrow OC20 + AQCat25	0.244	1.27
		31M in+midFiLM	OC20 + AQCat25	0.234	1.18
CHGNet		MPTrj	0.462	2.51	
DimeNet ⁺⁺		OC20 (All)	0.463	1.69	
EquiformerV2	31M	MPTrj	1.89	13.3	
		OMat24	3.32	18.5	
		OMat24 \rightarrow MPTrj + sAlex	3.34	19.4	
		OC20 (All+MD)	0.273	1.27	
	31M DeNS	MPTrj	2.18	14.7	
	83M	OC20 (2M)	0.431	1.57	
	86M	OMat24	3.28	18.4	
		OMat24 \rightarrow MPTrj + sAlex	3.34	19.3	
	86M DeNS	MPTrj	2.11	12.7	
	121M ($\lambda_E = 4, \lambda_F = 100$)	OC22	0.592	1.87	
153M	OMat24	3.33	19.1		
	OMat24 \rightarrow MPTrj + sAlex	3.35	19.3		
	OC20 (All+MD)	0.299	1.25		
	MPTrj	1.86	13.7		
eSCN	153M DeNS	MPTrj	1.86	13.7	
	$M = 2, 12$ layers	OC20 (All+MD)	0.315	1.31	
	$M = 3, 20$ layers	OC20 (All+MD)	0.340	1.38	
eSEN	30M	MPTrj	0.764	4.45	
		OMat24	2.43	15.0	
		OMat24 \rightarrow MPTrj + sAlex	2.62	15.3	
	small conserving	OC25	0.284	1.28	
	medium direct	OC25	0.305	1.32	

^a No strict neighbor enforcement.

Table S8: Prediction performance of the MLIPs for the reaction energy of RWGS reaction steps on metals and SAAs.

Model family	Variant	Training data set	RMSE (eV)	MaxAE (eV)
GemNet	dT	OC20 (All)	0.317	1.69
		OC22	1.42	4.93
	OC	OC20 (All)	0.291	1.43
		OC22	1.02	4.90
		OC20 + OC22	0.313	1.14
		OC20 \rightarrow OC22	0.827	2.98
OC ^a	OC20 + OC22	0.313	1.14	
GRACE	1 layer small	MPTrj	0.673	2.35
		OMat24	1.65	10.6
		OMat24 \rightarrow MPTrj + sAlex	2.16	13.7
	1 layer medium	OMat24	1.55	12.4
		OMat24 \rightarrow MPTrj + sAlex	1.53	12.6
	1 layer large	OMat24	1.52	11.6
		OMat24 \rightarrow MPTrj + sAlex	1.51	12.2
	2 layers small	MPTrj	0.521	2.35
		OMat24	1.48	10.6
		OMat24 \rightarrow MPTrj + sAlex	1.53	10.9
	2 layers medium	OMat24	1.53	10.6
		OMat24 \rightarrow MPTrj + sAlex	1.52	10.8
2 layers large	OMat24	1.43	10.1	
	OMat24 \rightarrow MPTrj + sAlex	1.53	10.8	
MACE	MP-0a small	MPTrj	0.913	5.00
	MP-0a medium	MPTrj	0.870	3.60
	MP-0a large	MPTrj	0.983	4.80
	MP-0b3 medium	MPTrj	0.694	3.32
	MPA-0 medium	MPTrj + sAlex	1.01	6.90
	OMAT-0 small	OMat24	1.53	12.9
	OMAT-0 medium	OMat24	2.03	15.3
	MatPES-PBE-0	MatPES-PBE	0.350	1.65
NequIP	L-0.1	MPTrj	0.750	4.13
		OMat24 \rightarrow MPTrj + sAlex	2.47	14.5
Orb	conservative, 20 neighbors	MPTrj + Alex	2.88	18.1
		OMat24 (only AIMD)	1.93	11.2
	conservative, ∞ neighbors	MPTrj + Alex	1.97	15.2
		OMat24 (only AIMD)	1.41	12.4
	direct, 20 neighbors	MPTrj + Alex	1.61	10.0
		OMat24 (only AIMD)	1.85	11.0
	direct, ∞ neighbors	MPTrj + Alex	1.59	10.0
		OMat24 (only AIMD)	1.55	10.9
PaiNN		OC20 (All)	0.420	1.50
SCN		OC20 (All+MD)	0.324	1.47
SevenNet	0	MPTrj	1.15	5.57
		OMat24	1.98	12.6
	13i5	MPTrj	0.954	4.16
		OMat24	1.89	15.9
MF	MPTrj + sAlex	2.08	17.5	
	OC20++	0.203	1.17	
UMA	S-1.1	OMat24	2.96	16.0
		OC20++	0.204	1.16
	M-1.1	OMat24	3.04	40.3
		OMat24 \rightarrow MPTrj + sAlex	1.21	9.25

^a No strict neighbor enforcement.

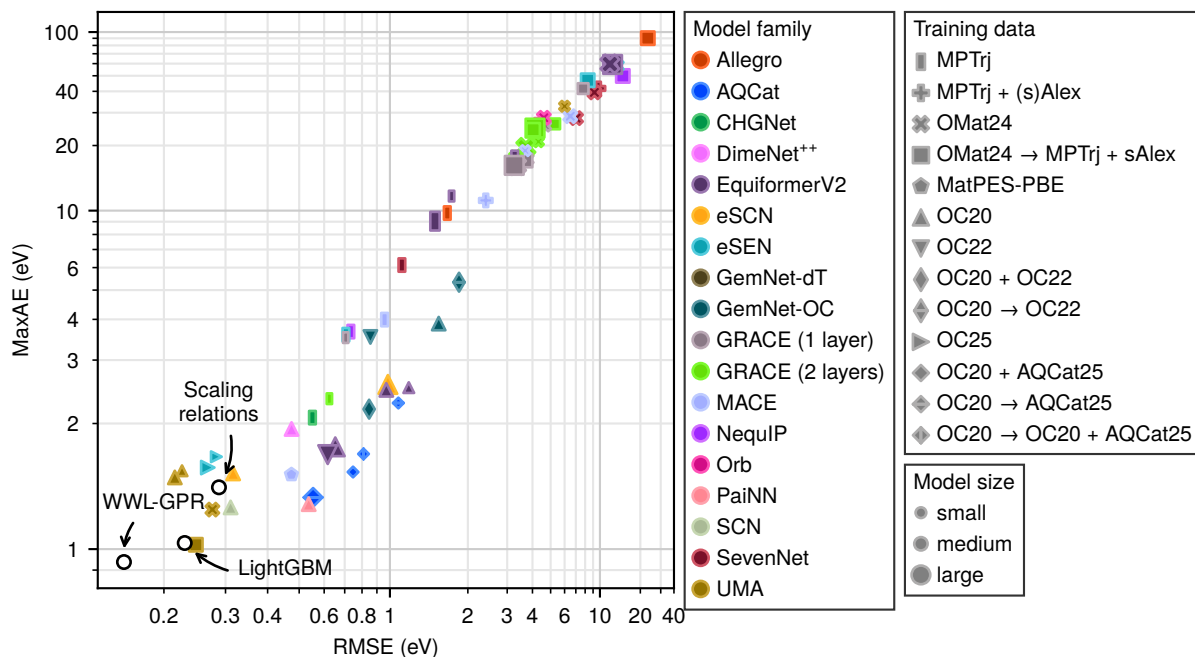


Figure S8: Prediction performance of the MLIPs for the formation energy of adsorbates of RWGS reaction steps on metals and SAAs.

Table S9: Prediction performance of the MLIPs for the formation energy of adsorbates of RWGS reaction steps on metals and SAAs.

Model family	Variant	Training data set	RMSE (eV)	MaxAE (eV)
Allegro	L-0.1	MPTrj	1.65	9.77
		OMat24 \rightarrow MPTrj + sAlex	23.1	90.2
AQCat	{ 31M 153M 31M inFiLM 31M in+midFiLM	OC20 \rightarrow AQCat25	1.07	2.27
		OC20 \rightarrow AQCat25	0.553	1.31
		OC20 \rightarrow OC20 + AQCat25	0.810	1.67
		OC20 + AQCat25	0.746	1.51
CHGNet		MPTrj	0.550	2.07
DimeNet ⁺⁺		OC20 (All)	0.474	1.94
EquiformerV2	31M	MPTrj	1.71	11.5
		OMat24	12.0	61.3
		OMat24 \rightarrow MPTrj + sAlex	12.5	60.5
		OC20 (All+MD)	1.17	2.50
	31M DeNS	MPTrj	3.57	16.2
		OC20 (2M)	0.971	2.47
	86M	OMat24	11.9	60.8
		OMat24 \rightarrow MPTrj + sAlex	12.3	60.0
86M DeNS	MPTrj	3.26	17.5	
121M ($\lambda_E = 4, \lambda_F = 100$)	OC22	0.616	1.66	
153M	OMat24	11.7	59.6	
	OMat24 \rightarrow MPTrj + sAlex	12.2	59.2	
	OC20 (All+MD)	0.652	1.74	
	MPTrj	1.47	9.04	
eSCN	{ $M = 2, 12$ layers $M = 3, 20$ layers	OC20 (All+MD)	0.316	1.50
		OC20 (All+MD)	0.984	2.55

^a No strict neighbor enforcement.

Table S9: Prediction performance of the MLIPs for the formation energy of adsorbates of RWGS reaction steps on metals and SAAs.

Model family	Variant	Training data set	RMSE (eV)	MaxAE (eV)
eSEN	30M	MPTrj	0.706	3.58
		OMat24	13.1	58.1
		OMat24 \rightarrow MPTrj + sAlex	8.30	46.8
	small conserving medium direct	OC25	0.282	1.64
		OC25	0.267	1.55
GemNet	dT	OC20 (All)	–	–
		OC22	–	–
	OC	OC20 (All)	1.52	3.88
		OC22	0.854	3.52
		OC20 + OC22	0.846	2.18
	OC ^a	OC20 \rightarrow OC22	1.84	5.32
		OC20 + OC22	0.846	2.18
GRACE	1 layer small	MPTrj	0.705	3.51
		OMat24	4.69	25.3
		OMat24 \rightarrow MPTrj + sAlex	7.77	41.6
	1 layer medium	OMat24	3.74	17.1
		OMat24 \rightarrow MPTrj + sAlex	3.69	16.8
	1 layer large	OMat24	3.33	15.9
		OMat24 \rightarrow MPTrj + sAlex	3.24	16.0
	2 layers small	MPTrj	0.624	2.33
		OMat24	4.30	20.9
		OMat24 \rightarrow MPTrj + sAlex	5.27	26.0
		OMat24	3.30	17.4
	2 layers medium	OMat24 \rightarrow MPTrj + sAlex	4.03	24.2
		OMat24	3.70	19.5
	2 layers large	OMat24 \rightarrow MPTrj + sAlex	4.12	24.7
MP-0a small		MPTrj	1.32	6.52
MACE	MP-0a medium	MPTrj	1.09	5.61
	MP-0a large	MPTrj	1.15	6.28
	MP-0b3 medium	MPTrj	0.957	3.99
	MPA-0 medium	MPTrj + sAlex	2.39	11.1
	OMAT-0 small	OMat24	3.67	18.8
	OMAT-0 medium	OMat24	6.48	28.7
	MatPES-PBE-0	MatPES-PBE	0.473	1.49
	NequIP	L-0.1	MPTrj	0.734
OMat24 \rightarrow MPTrj + sAlex			14.6	49.9
Orb	conservative, 20 neighbors	MPTrj + Alex	12.4	53.0
		OMat24 (only AIMD)	7.60	38.3
	conservative, ∞ neighbors	MPTrj + Alex	12.4	47.8
		OMat24 (only AIMD)	7.05	33.5
	direct, 20 neighbors	MPTrj + Alex	6.23	27.2
		OMat24 (only AIMD)	7.37	32.1
	direct, ∞ neighbors	MPTrj + Alex	4.22	25.7
		OMat24 (only AIMD)	4.59	28.1
PaiNN		OC20 (All)	0.536	1.26
SCN		OC20 (All+MD)	0.310	1.24
SevenNet	0	MPTrj	1.11	8.59
		OMat24	7.03	28.0
	l3i5	MPTrj	1.10	6.13
		OMat24	9.18	39.4
	MF	MPTrj + sAlex	9.78	41.7

^a No strict neighbor enforcement.

Table S9: Prediction performance of the MLIPs for the formation energy of adsorbates of RWGS reaction steps on metals and SAAs.

Model family	Variant	Training data set	RMSE (eV)	MaxAE (eV)
UMA	S-1.1	OC20++	0.225	1.52
		OMat24	6.00	32.7
	M-1.1	OC20++	0.215	1.46
		OMat24	0.275	1.23
		OMat24 \rightarrow MPTrj + sAlex	0.246	1.02
Scaling relations [2]			0.287	1.39
LightGBM [2]			0.229	1.03
WWL-GPR [2]			0.155	0.937

^a No strict neighbor enforcement.

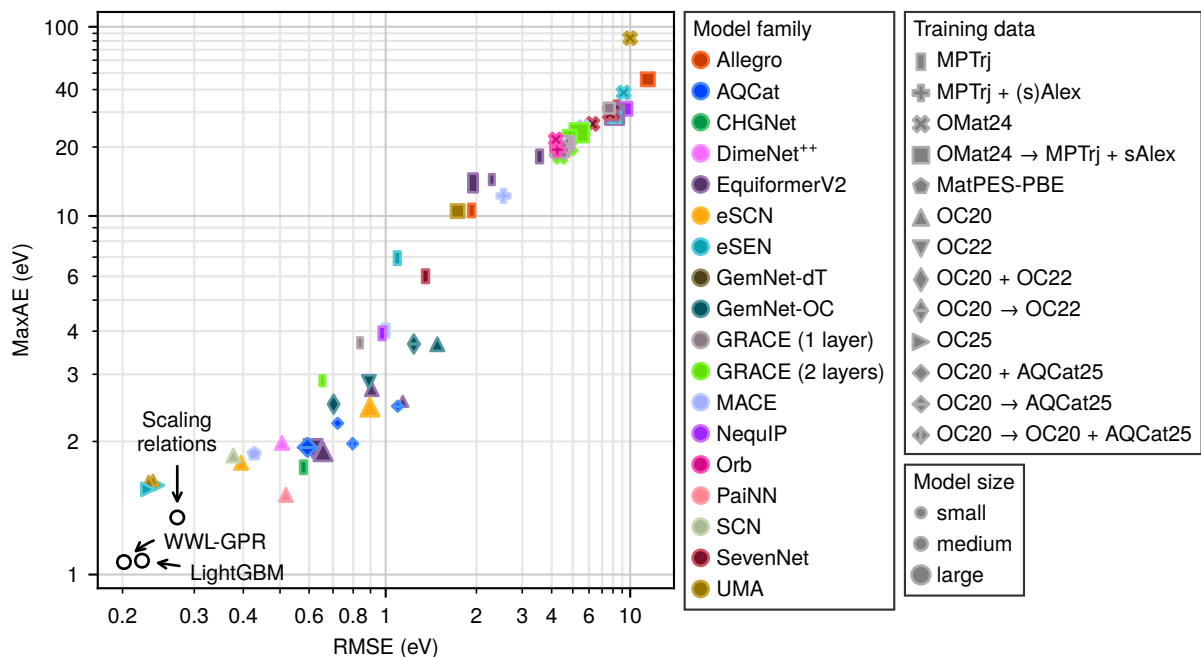


Figure S9: Prediction performance of the MLIPs for the formation energy of TSs of RWGS reaction steps on metals and SAAs.

Table S10: Prediction performance of the MLIPs for the formation energy of TSs of RWGS reaction steps on metals and SAAs.

Model family	Variant	Training data set	RMSE (eV)	MaxAE (eV)
Allegro	L-0.1	MPTrj	1.92	10.5
		OMat24 \rightarrow MPTrj + sAlex	12.8	45.9
AQCat	31M	OC20 \rightarrow AQCat25	1.09	2.46
		OC20 \rightarrow AQCat25	0.593	1.93
		OC20 \rightarrow OC20 + AQCat25	0.797	1.98
		OC20 + AQCat25	0.721	2.22
CHGNet		MPTrj	0.579	1.73
DimeNet ⁺⁺		OC20 (All)	0.506	1.98
EquiformerV2	31M	MPTrj	2.28	14.2
		OMat24	8.19	31.0
		OMat24 \rightarrow MPTrj + sAlex	8.30	29.7
		OC20 (All+MD)	1.13	2.53
	31M DeNS	MPTrj	3.87	19.6
		OC20 (2M)	0.907	2.73
	86M	OMat24	8.15	30.3
		OMat24 \rightarrow MPTrj + sAlex	8.19	28.9
	86M DeNS	MPTrj	3.54	18.0
		OC22	0.615	1.92
121M ($\lambda_E = 4, \lambda_F = 100$)	153M	OMat24	7.95	29.9
		OMat24 \rightarrow MPTrj + sAlex	8.16	28.9
	OC20 (All+MD)	0.656	1.89	
153M DeNS	MPTrj	1.94	13.7	
	eSCN	OC20 (All+MD)	0.395	1.77
		OC20 (All+MD)	0.896	2.45

^a No strict neighbor enforcement.

Table S10: Prediction performance of the MLIPs for the formation energy of TSs of RWGS reaction steps on metals and SAAs.

Model family	Variant	Training data set	RMSE (eV)	MaxAE (eV)
eSEN	30M	MPTrj	1.09	6.94
		OMat24	9.16	38.4
		OMat24 \rightarrow MPTrj + sAlex	8.13	28.6
	small conserving medium direct	OC25	0.245	1.57
OC25		0.231	1.54	
GemNet	dT	OC20 (All)	–	–
		OC22	–	–
	OC	OC20 (All)	1.46	3.66
		OC22	0.890	2.86
		OC20 + OC22	0.702	2.49
		OC20 \rightarrow OC22	1.22	3.66
OC ^a	OC20 + OC22	0.702	2.49	
GRACE	1 layer small	MPTrj	0.838	3.69
		OMat24	5.44	24.2
		OMat24 \rightarrow MPTrj + sAlex	7.64	31.5
	1 layer medium	OMat24	4.69	20.5
		OMat24 \rightarrow MPTrj + sAlex	4.71	20.9
	1 layer large	OMat24	4.33	19.3
		OMat24 \rightarrow MPTrj + sAlex	4.36	19.9
	2 layers small	MPTrj	0.653	2.88
		OMat24	4.82	21.6
		OMat24 \rightarrow MPTrj + sAlex	5.65	24.1
		OMat24	4.37	18.0
	2 layers medium	OMat24 \rightarrow MPTrj + sAlex	4.84	22.4
OMat24		4.75	20.3	
2 layers large	OMat24 \rightarrow MPTrj + sAlex	5.37	23.5	
	MP-0a small	MPTrj	1.60	7.11
MACE	MP-0a medium	MPTrj	1.34	6.59
	MP-0a large	MPTrj	1.47	7.56
	MP-0b3 medium	MPTrj	1.00	4.02
	MPA-0 medium	MPTrj + sAlex	2.53	12.1
	OMAT-0 small	OMat24	4.34	21.1
	OMAT-0 medium	OMat24	5.62	25.1
	MatPES-PBE-0	MatPES-PBE	0.427	1.87
	NequIP	L-0.1	MPTrj	0.975
OMat24 \rightarrow MPTrj + sAlex			9.38	31.3
Orb	conservative, 20 neighbors	MPTrj + Alex	7.95	28.8
		OMat24 (only AIMD)	5.57	26.9
	conservative, ∞ neighbors	MPTrj + Alex	8.64	32.1
		OMat24 (only AIMD)	6.06	26.2
	direct, 20 neighbors	MPTrj + Alex	4.84	25.6
		OMat24 (only AIMD)	5.28	27.3
direct, ∞ neighbors	MPTrj + Alex	4.24	19.4	
	OMat24 (only AIMD)	4.18	21.8	
PaiNN		OC20 (All)	0.518	1.49
SCN		OC20 (All+MD)	0.377	1.85
SevenNet	0	MPTrj	1.42	8.17
		OMat24	6.23	26.0
	l3i5	MPTrj	1.34	6.00
		OMat24	7.72	29.4
	MF	MPTrj + sAlex	8.35	31.9

^a No strict neighbor enforcement.

Table S10: Prediction performance of the MLIPs for the formation energy of TSs of RWGS reaction steps on metals and SAAs.

Model family	Variant	Training data set	RMSE (eV)	MaxAE (eV)
UMA	S-1.1	OC20++	0.237	1.61
		OMat24	7.95	31.3
	M-1.1	OC20++	0.231	1.59
		OMat24	9.99	83.5
		OMat24 \rightarrow MPTrj + sAlex	1.72	10.5
	Scaling relations [2]			0.272
LightGBM [2]			0.223	1.07
WWL-GPR [2]			0.202	1.06

^a No strict neighbor enforcement.

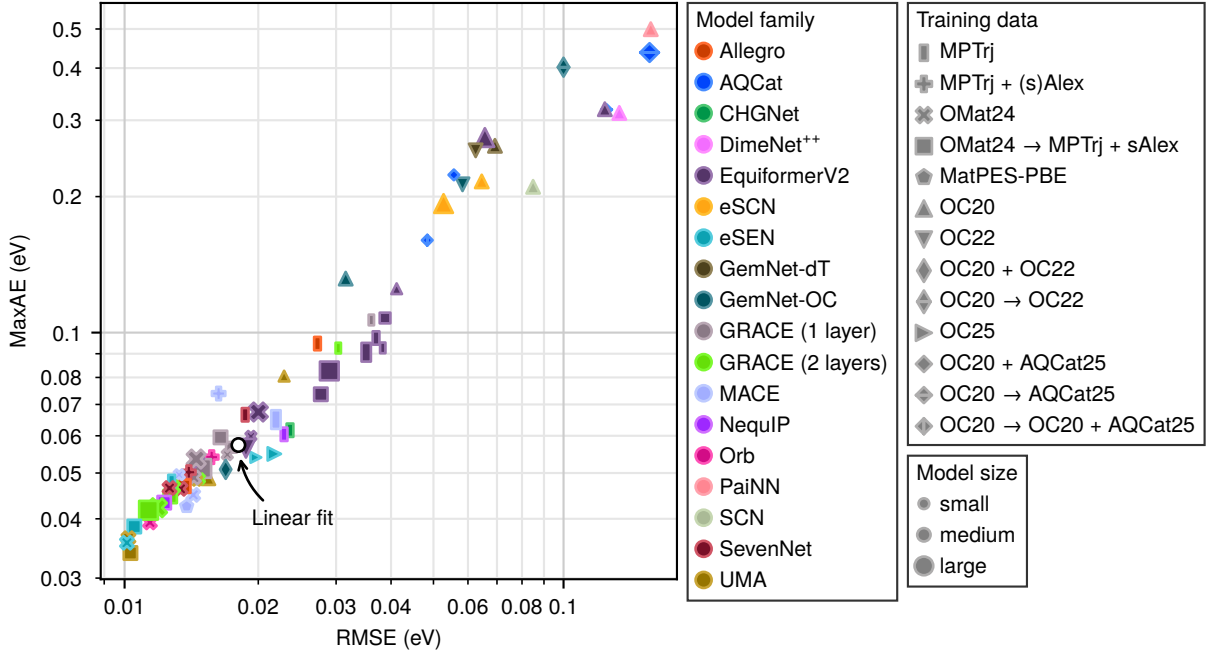


Figure S10: Prediction performance of the MLIPs for the zero-point energy of metal oxide nanoclusters on metal supports.

Table S11: Prediction performance of the MLIPs for the zero-point energy of metal oxide nanoclusters on metal supports.

Model family	Variant	Training data set	RMSE (eV)	MaxAE (eV)
Allegro	L-0.1	MPTrj	0.0272	0.0947
		OMat24 \rightarrow MPTrj + sAlex	0.0136	0.0469
AQCat	31M	OC20 \rightarrow AQCat25	0.126	0.318
	153M	OC20 \rightarrow AQCat25	0.160	0.437
	31M inFiLM	OC20 \rightarrow OC20 + AQCat25	0.0484	0.160
	31M in+midFiLM	OC20 + AQCat25	0.0557	0.224
CHGNet		MPTrj	0.0236	0.0617
DimeNet ⁺⁺		OC20 (All)	0.135	0.312
EquiformerV2	31M	MPTrj	0.0383	0.0927
		OMat24	0.0192	0.0598
		OMat24 \rightarrow MPTrj + sAlex	0.0388	0.108
		OC20 (All+MD)	0.0412	0.125
	31M DeNS	MPTrj	0.0605	0.185
	83M	OC20 (2M)	0.125	0.319
	86M	OMat24	0.0146	0.0529
		OMat24 \rightarrow MPTrj + sAlex	0.0277	0.0736
		MPTrj	0.0370	0.0973
	121M ($\lambda_E = 4, \lambda_F = 100$)	OC22	0.0188	0.0564
153M	OMat24	0.0200	0.0674	
	OMat24 \rightarrow MPTrj + sAlex	0.0290	0.0826	
	OC20 (All+MD)	0.0656	0.273	
	MPTrj	0.0351	0.0907	
	OC20 (All+MD)	0.0645	0.217	
eSCN	$M = 2, 12$ layers	OC20 (All+MD)	0.0527	0.193
	$M = 3, 20$ layers	OC20 (All+MD)	0.0527	0.193
eSEN	30M	MPTrj	0.0128	0.0480
		OMat24	0.0101	0.0356
		OMat24 \rightarrow MPTrj + sAlex	0.0105	0.0385
	small conserving	OC25	0.0198	0.0540
	medium direct	OC25	0.0217	0.0549

^a No strict neighbor enforcement.

Table S11: Prediction performance of the MLIPs for the zero-point energy of metal oxide nanoclusters on metal supports.

Model family	Variant	Training data set	RMSE (eV)	MaxAE (eV)
GemNet	dT	OC20 (All)	0.0692	0.261
		OC22	0.0625	0.255
	OC	OC20 (All)	0.0315	0.131
		OC22	0.0583	0.213
		OC20 + OC22	0.0169	0.0509
		OC20 \rightarrow OC22	0.100	0.402
OC ^a	OC20 + OC22	0.0169	0.0509	
GRACE	1 layer small	MPTrj	0.0361	0.107
		OMat24	0.0170	0.0547
		OMat24 \rightarrow MPTrj + sAlex	0.0174	0.0567
	1 layer medium	OMat24	0.0143	0.0489
		OMat24 \rightarrow MPTrj + sAlex	0.0164	0.0595
	1 layer large	OMat24	0.0145	0.0535
		OMat24 \rightarrow MPTrj + sAlex	0.0149	0.0511
	2 layers small	MPTrj	0.0303	0.0926
		OMat24	0.0147	0.0486
		OMat24 \rightarrow MPTrj + sAlex	0.0136	0.0469
	2 layers medium	OMat24	0.0129	0.0467
		OMat24 \rightarrow MPTrj + sAlex	0.0127	0.0446
2 layers large	OMat24	0.0119	0.0422	
	OMat24 \rightarrow MPTrj + sAlex	0.0113	0.0417	
MACE	MP-0a small	MPTrj	0.0227	0.0525
	MP-0a medium	MPTrj	0.0248	0.0748
	MP-0a large	MPTrj	0.0219	0.0650
	MP-0b3 medium	MPTrj	0.0233	0.0899
	MPA-0 medium	MPTrj + sAlex	0.0163	0.0739
	OMAT-0 small	OMat24	0.0133	0.0496
	OMAT-0 medium	OMat24	0.0143	0.0449
	MatPES-PBE-0	MatPES-PBE	0.0138	0.0425
NequIP	L-0.1	MPTrj	0.0229	0.0604
		OMat24 \rightarrow MPTrj + sAlex	0.0123	0.0433
Orb	conservative, 20 neighbors	MPTrj + Alex	0.0181	0.0566
		OMat24 (only AIMD)	0.0136	0.0426
	conservative, ∞ neighbors	MPTrj + Alex	0.0157	0.0540
		OMat24 (only AIMD)	0.0114	0.0393
	direct, 20 neighbors	MPTrj + Alex	0.0353	0.0813
		OMat24 (only AIMD)	0.0173	0.0414
	direct, ∞ neighbors	MPTrj + Alex	0.0224	0.0641
		OMat24 (only AIMD)	0.0131	0.0394
PaiNN		OC20 (All)	0.161	0.499
SCN		OC20 (All+MD)	0.0849	0.211
SevenNet	0	MPTrj	0.0262	0.0983
		OMat24	0.0134	0.0463
	13i5	MPTrj	0.0187	0.0665
		OMat24	0.0126	0.0465
MF	MPTrj + sAlex	0.0139	0.0502	
	OC20++	0.0229	0.0805	
UMA	S-1.1	OMat24	0.0145	0.0483
		OC20++	0.0154	0.0487
	M-1.1	OMat24	0.0102	0.0364
		OMat24 \rightarrow MPTrj + sAlex	0.0103	0.0339
Linear fit [3, 4]			0.0180	0.0573

^a No strict neighbor enforcement.

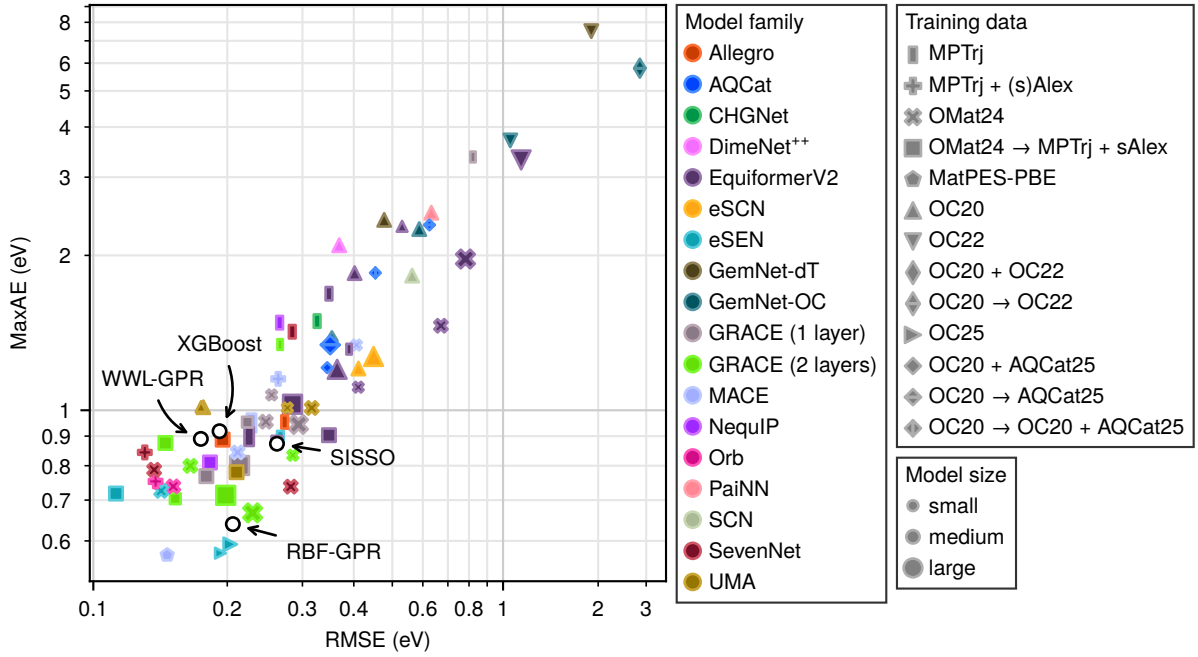


Figure S11: Prediction performance of the MLIPs for the adsorption energy of formate on metal-supported metal oxide nanoclusters.

Table S12: Prediction performance of the MLIPs for the adsorption energy of formate on metal-supported metal oxide nanoclusters.

Model family	Variant	Training data set	RMSE (eV)	MaxAE (eV)
Allegro	L-0.1	MPTrj	0.272	0.953
		OMat24 \rightarrow MPTrj + sAlex	0.195	0.887
AQCat	{ 31M 153M 31M inFiLM 31M in+midFiLM	OC20 \rightarrow AQCat25	0.625	2.33
		OC20 \rightarrow AQCat25	0.350	1.32
		OC20 \rightarrow OC20 + AQCat25	0.453	1.84
		OC20 + AQCat25	0.344	1.20
CHGNet		MPTrj	0.325	1.47
DimeNet ⁺⁺		OC20 (All)	0.368	2.10
EquiformerV2	31M	MPTrj	0.389	1.30
		OMat24	0.410	1.10
		OMat24 \rightarrow MPTrj + sAlex	0.261	0.882
		OC20 (All+MD)	0.530	2.31
	31M DeNS	MPTrj	0.493	1.30
		OC20 (2M)	0.402	1.84
	86M	OMat24	0.670	1.44
		OMat24 \rightarrow MPTrj + sAlex	0.348	0.903
	86M DeNS	MPTrj	0.348	1.67
		121M ($\lambda_E = 4, \lambda_F = 100$)	OC22	1.13
153M		OMat24	0.782	1.97
		OMat24 \rightarrow MPTrj + sAlex	0.284	1.03
		OC20 (All+MD)	0.364	1.19
153M DeNS		MPTrj	0.225	0.898
		OC20 (All+MD)	0.411	1.19
		OC20 (All+MD)	0.448	1.26

^a No strict neighbor enforcement.

Table S12: Prediction performance of the MLIPs for the adsorption energy of formate on metal-supported metal oxide nanoclusters.

Model family	Variant	Training data set	RMSE (eV)	MaxAE (eV)
eSEN	30M	MPTrj	0.266	0.895
		OMat24	0.142	0.725
		OMat24 \rightarrow MPTrj + sAlex	0.112	0.718
	small conserving medium direct	OC25	0.193	0.573
		OC25	0.203	0.592
GemNet	dT	OC20 (All)	0.477	2.39
		OC22	1.89	7.50
	OC	OC20 (All)	0.587	2.28
		OC22	1.05	3.69
		OC20 + OC22	0.353	1.34
		OC20 \rightarrow OC22	2.83	5.80
	OC ^a	OC20 + OC22	0.353	1.34
	GRACE	1 layer small	MPTrj	0.820
OMat24			0.254	1.07
OMat24 \rightarrow MPTrj + sAlex			0.223	0.953
1 layer medium		OMat24	0.246	0.954
		OMat24 \rightarrow MPTrj + sAlex	0.179	0.768
1 layer large		OMat24	0.293	0.944
		OMat24 \rightarrow MPTrj + sAlex	0.214	0.801
2 layers small		MPTrj	0.266	1.32
		OMat24	0.285	0.834
		OMat24 \rightarrow MPTrj + sAlex	0.152	0.704
		OMat24	0.165	0.799
2 layers medium		OMat24 \rightarrow MPTrj + sAlex	0.145	0.875
	OMat24	0.229	0.667	
2 layers large	OMat24 \rightarrow MPTrj + sAlex	0.198	0.713	
	MP-0a small	MPTrj	0.314	1.16
MACE	MP-0a medium	MPTrj	0.322	1.07
	MP-0a large	MPTrj	0.228	0.949
	MP-0b3 medium	MPTrj	0.333	1.17
	MPA-0 medium	MPTrj + sAlex	0.263	1.14
	OMAT-0 small	OMat24	0.406	1.32
	OMAT-0 medium	OMat24	0.211	0.843
	MatPES-PBE-0	MatPES-PBE	0.146	0.569
	NequIP	L-0.1	MPTrj	0.265
OMat24 \rightarrow MPTrj + sAlex			0.183	0.810
Orb	conservative, 20 neighbors	MPTrj + Alex	0.160	0.796
		OMat24 (only AIMD)	0.236	0.957
	conservative, ∞ neighbors	MPTrj + Alex	0.138	0.752
		OMat24 (only AIMD)	0.151	0.738
	direct, 20 neighbors	MPTrj + Alex	0.150	0.762
		OMat24 (only AIMD)	0.294	0.889
	direct, ∞ neighbors	MPTrj + Alex	0.146	0.616
		OMat24 (only AIMD)	0.258	1.24
PaiNN		OC20 (All)	0.632	2.48
SCN		OC20 (All+MD)	0.563	1.81
SevenNet	0	MPTrj	0.284	1.40
		OMat24	0.281	0.737
	l3i5	MPTrj	0.377	1.23
		OMat24	0.137	0.787
	MF	MPTrj + sAlex	0.130	0.843

^a No strict neighbor enforcement.

Table S12: Prediction performance of the MLIPs for the adsorption energy of formate on metal-supported metal oxide nanoclusters.

Model family	Variant	Training data set	RMSE (eV)	MaxAE (eV)
UMA	S-1.1	OC20++	0.174	1.02
		OMat24	0.276	1.01
	M-1.1	OC20++	0.176	1.01
		OMat24	0.316	1.01
		OMat24 \rightarrow MPTrj + sAlex	0.210	0.780
RBF-GPR [5]		0.206	0.639	
XGBoost [5]		0.192	0.918	
SISSO [5]		0.261	0.873	
WWL-GPR [5]		0.174	0.890	

^a No strict neighbor enforcement.

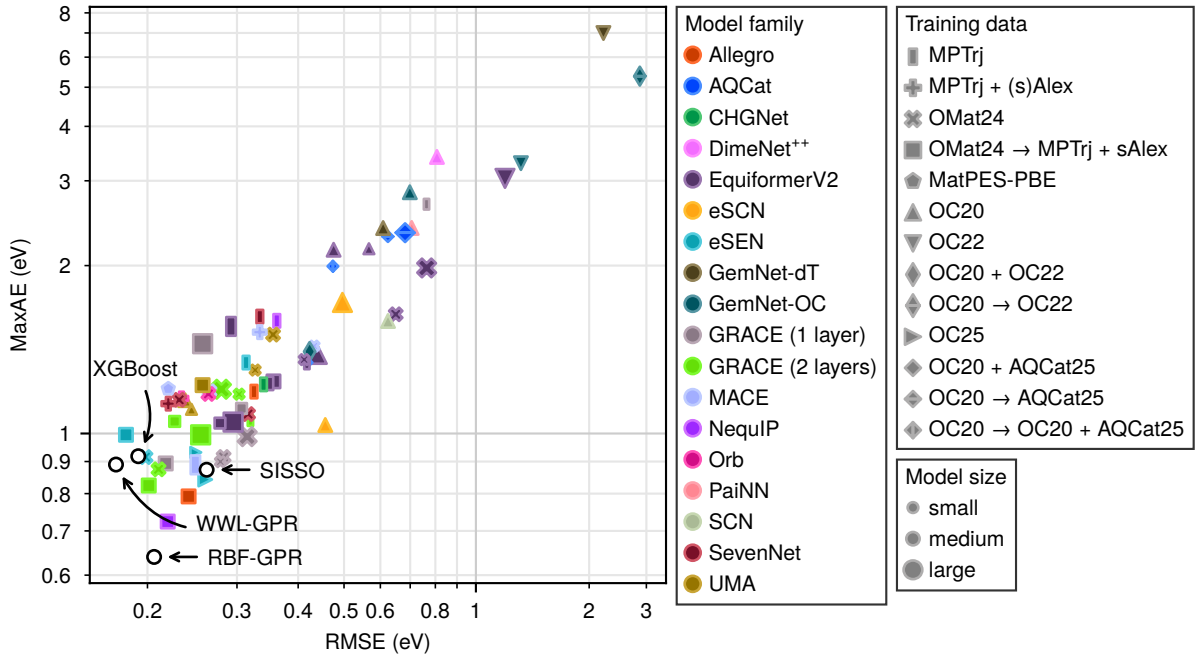


Figure S12: Prediction performance of the MLIPs for the adsorption energy of formate on metal-supported metal oxide nanoclusters, after relaxing into the local minimum for each MLIP.

Table S13: Prediction performance of the MLIPs for the adsorption energy of formate on metal-supported metal oxide nanoclusters, after relaxing into the local minimum for each MLIP.

Model family	Variant	Training data set	RMSE (eV)	MaxAE (eV)
Allegro	L-0.1	MPTrj	0.325	1.18
		OMat24 \rightarrow MPTrj + sAlex	0.240	0.792
AQCat	31M	OC20 \rightarrow AQCat25	0.624	2.29
	153M	OC20 \rightarrow AQCat25	0.682	2.33
	31M inFiLM	OC20 \rightarrow OC20 + AQCat25	0.473	1.99
	31M in+midFiLM	OC20 + AQCat25	0.417	1.32
CHGNet		MPTrj	0.340	1.21
DimeNet ⁺⁺		OC20 (All)	0.807	3.39
	31M	MPTrj	0.417	1.31
OMat24		0.412	1.34	
OMat24 \rightarrow MPTrj + sAlex		0.277	1.04	
OC20 (All+MD)		0.566	2.16	
EquiformerV2	31M DeNS	MPTrj	0.500	1.33
	83M	OC20 (2M)	0.475	2.15
	86M	OMat24	0.649	1.61
EquiformerV2	86M	OMat24 \rightarrow MPTrj + sAlex	0.356	1.22
		MPTrj	0.350	1.21
	121M ($\lambda_E = 4, \lambda_F = 100$)	OC22	1.18	3.04
	153M	OMat24	0.764	1.98
eSCN	153M DeNS	OMat24 \rightarrow MPTrj + sAlex	0.295	1.04
		OC20 (All+MD)	0.439	1.37
	MPTrj	0.292	1.53	
	$M = 2, 12$ layers	OC20 (All+MD)	0.456	1.03
$M = 3, 20$ layers	OC20 (All+MD)	0.496	1.70	

^a No strict neighbor enforcement.

Table S13: Prediction performance of the MLIPs for the adsorption energy of formate on metal-supported metal oxide nanoclusters, after relaxing into the local minimum for each MLIP.

Model family	Variant	Training data set	RMSE (eV)	MaxAE (eV)
eSEN	30M	MPTrj	0.313	1.32
		OMat24	0.198	0.915
		OMat24 \rightarrow MPTrj + sAlex	0.182	0.995
	small conserving medium direct	OC25	0.248	0.931
		OC25	0.259	0.842
GemNet	dT	OC20 (All)	0.609	2.38
		OC22	2.20	7.00
	OC	OC20 (All)	0.699	2.83
		OC22	1.30	3.28
		OC20 + OC22	0.425	1.38
	OC ^a	OC20 \rightarrow OC22	2.86	5.34
		OC20 + OC22	0.423	1.38
GRACE	1 layer small	MPTrj	0.763	2.67
		OMat24	0.278	0.900
		OMat24 \rightarrow MPTrj + sAlex	0.306	1.10
	1 layer medium	OMat24	0.282	0.915
		OMat24 \rightarrow MPTrj + sAlex	0.217	0.894
	1 layer large	OMat24	0.314	0.988
		OMat24 \rightarrow MPTrj + sAlex	0.256	1.43
	2 layers small	MPTrj	0.319	1.05
		OMat24	0.303	1.16
		OMat24 \rightarrow MPTrj + sAlex	0.226	1.05
	2 layers medium	OMat24	0.210	0.874
		OMat24 \rightarrow MPTrj + sAlex	0.201	0.824
	2 layers large	OMat24	0.279	1.19
		OMat24 \rightarrow MPTrj + sAlex	0.254	0.995
MACE	MP-0a small	MPTrj	0.322	1.11
	MP-0a medium	MPTrj	0.311	1.65
	MP-0a large	MPTrj	0.248	0.889
	MP-0b3 medium	MPTrj	0.395	1.64
	MPA-0 medium	MPTrj + sAlex	0.334	1.50
	OMAT-0 small	OMat24	0.432	1.41
	OMAT-0 medium	OMat24	0.264	1.18
	MatPES-PBE-0	MatPES-PBE	0.219	1.19
NequIP	L-0.1	MPTrj	0.361	1.57
		OMat24 \rightarrow MPTrj + sAlex	0.219	0.724
Orb	conservative, 20 neighbors	MPTrj + Alex	0.237	1.18
		OMat24 (only AIMD)	0.271	0.801
	conservative, ∞ neighbors	MPTrj + Alex	0.233	1.15
		OMat24 (only AIMD)	0.263	1.17
	direct, 20 neighbors	MPTrj + Alex	0.238	1.18
		OMat24 (only AIMD)	0.354	1.48
	direct, ∞ neighbors	MPTrj + Alex	0.233	1.16
		OMat24 (only AIMD)	0.310	1.29
PaiNN		OC20 (All)	0.706	2.38
SCN		OC20 (All+MD)	0.624	1.57
SevenNet	0	MPTrj	0.334	1.60
		OMat24	0.316	1.08
	l3i5	MPTrj	0.481	1.67
		OMat24	0.231	1.14
	MF	MPTrj + sAlex	0.219	1.12

^a No strict neighbor enforcement.

Table S13: Prediction performance of the MLIPs for the adsorption energy of formate on metal-supported metal oxide nanoclusters, after relaxing into the local minimum for each MLIP.

Model family	Variant	Training data set	RMSE (eV)	MaxAE (eV)
UMA	S-1.1	OC20++	0.244	1.10
		OMat24	0.326	1.28
	M-1.1	OC20++	0.237	1.14
		OMat24	0.355	1.48
		OMat24 \rightarrow MPTrj + sAlex	0.256	1.21
RBF-GPR [5]		0.206	0.639	
XGBoost [5]		0.192	0.918	
SISSO [5]		0.261	0.873	
WWL-GPR [5]		0.174	0.890	

^a No strict neighbor enforcement.

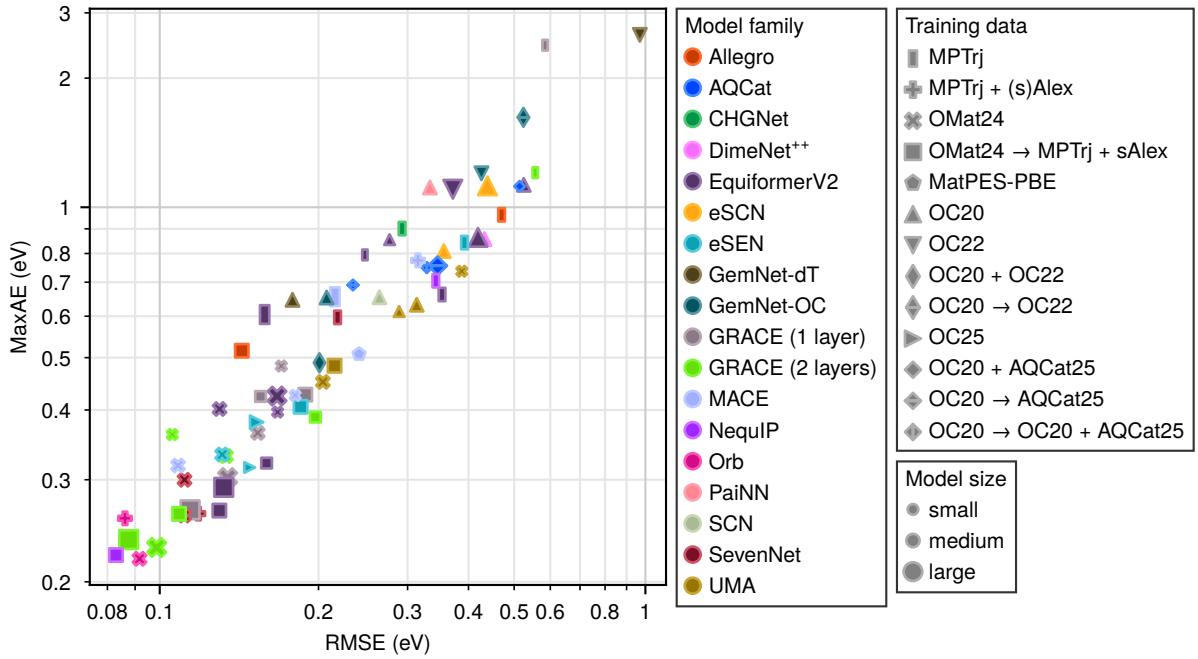


Figure S13: Prediction performance of the MLIPs for the activation energy of the $\text{CO}_2 + \text{H} \rightleftharpoons \text{HCOO}$ reaction step on metal-supported metal oxide nanoclusters.

Table S14: Prediction performance of the MLIPs for the activation energy of the $\text{CO}_2 + \text{H} \rightleftharpoons \text{HCOO}$ reaction step on metal-supported metal oxide nanoclusters.

Model family	Variant	Training data set	RMSE (eV)	MaxAE (eV)	
Allegro	L-0.1	MPTrj	0.470	0.964	
		OMat24 \rightarrow MPTrj + sAlex	0.143	0.515	
AQCat	31M	OC20 \rightarrow AQCat25	0.234	0.691	
		153M	OC20 \rightarrow AQCat25	0.345	0.755
		31M inFiLM	OC20 \rightarrow OC20 + AQCat25	0.328	0.749
		31M in+midFiLM	OC20 + AQCat25	0.514	1.11
CHGNet		MPTrj	0.292	0.901	
DimeNet ⁺⁺		OC20 (All)	0.432	0.857	
EquiformerV2	31M	MPTrj	0.571	1.07	
		OMat24	0.167	0.396	
		OMat24 \rightarrow MPTrj + sAlex	0.159	0.321	
		OC20 (All+MD)	0.276	0.855	
	31M DeNS	MPTrj	0.247	0.795	
		83M	OC20 (2M)	0.525	1.12
	86M	OMat24	0.129	0.402	
		OMat24 \rightarrow MPTrj + sAlex	0.129	0.265	
		86M DeNS	MPTrj	0.353	0.662
		121M ($\lambda_E = 4, \lambda_F = 100$)	OC22	0.371	1.09
153M	OMat24	0.166	0.424		
	OMat24 \rightarrow MPTrj + sAlex	0.132	0.291		
	OC20 (All+MD)	0.419	0.864		
	153M DeNS	MPTrj	0.158	0.605	
eSCN	$M = 2, 12$ layers	OC20 (All+MD)	0.356	0.809	
		$M = 3, 20$ layers	OC20 (All+MD)	0.438	1.11
eSEN	30M	MPTrj	0.392	0.842	
		OMat24	0.131	0.332	
		OMat24 \rightarrow MPTrj + sAlex	0.185	0.405	
	small conserving	OC25	0.148	0.315	
	medium direct	OC25	0.152	0.380	

^a No strict neighbor enforcement.

Table S14: Prediction performance of the MLIPs for the activation energy of the $\text{CO}_2 + \text{H} \rightleftharpoons \text{HCOO}$ reaction step on metal-supported metal oxide nanoclusters.

Model family	Variant	Training data set	RMSE (eV)	MaxAE (eV)
GemNet	dT	OC20 (All)	0.178	0.646
		OC22	0.969	2.60
	OC	OC20 (All)	0.207	0.653
		OC22	0.426	1.19
		OC20 + OC22	0.201	0.489
GRACE	OC ^a	OC20 \rightarrow OC22	0.524	1.60
	1 layer small	OC20 + OC22	0.201	0.489
		MPTrj	0.584	2.44
	1 layer medium	OMat24	0.170	0.482
		OMat24 \rightarrow MPTrj + sAlex	0.155	0.423
	1 layer large	OMat24	0.153	0.363
		OMat24 \rightarrow MPTrj + sAlex	0.189	0.427
	2 layers small	OMat24	0.134	0.303
		OMat24 \rightarrow MPTrj + sAlex	0.114	0.266
		MPTrj	0.556	1.19
OMat24		0.106	0.361	
2 layers medium	OMat24 \rightarrow MPTrj + sAlex	0.197	0.388	
	OMat24	0.133	0.330	
2 layers large	OMat24 \rightarrow MPTrj + sAlex	0.109	0.261	
	OMat24	0.0987	0.229	
MACE	MP-0a small	OMat24 \rightarrow MPTrj + sAlex	0.0876	0.236
	MP-0a medium	MPTrj	0.426	1.32
	MP-0a large	MPTrj	0.432	0.904
	MP-0b3 medium	MPTrj	0.215	0.655
	MPA-0 medium	MPTrj	0.330	0.810
	OMAT-0 small	MPTrj + sAlex	0.315	0.775
	OMAT-0 medium	OMat24	0.180	0.425
	MatPES-PBE-0	OMat24	0.108	0.318
NequIP	L-0.1	MatPES-PBE	0.240	0.508
		MPTrj	0.342	0.705
Orb	conservative, 20 neighbors	OMat24 \rightarrow MPTrj + sAlex	0.0830	0.222
		MPTrj + Alex	0.156	0.323
	conservative, ∞ neighbors	OMat24 (only AIMD)	0.185	0.390
		MPTrj + Alex	0.125	0.257
	direct, 20 neighbors	OMat24 (only AIMD)	0.0917	0.219
		MPTrj + Alex	0.168	0.359
	direct, ∞ neighbors	OMat24 (only AIMD)	0.189	0.456
		MPTrj + Alex	0.0862	0.257
PaiNN	SCN	OMat24 (only AIMD)	0.172	0.528
		OC20 (All)	0.333	1.10
SevenNet	0	OC20 (All+MD)	0.263	0.654
		MPTrj	0.218	0.597
	13i5	OMat24	0.111	0.300
		MPTrj	0.294	0.620
	MF	OMat24	0.111	0.260
MPTrj + sAlex		0.118	0.262	
UMA	S-1.1	OC20++	0.288	0.613
		OMat24	0.387	0.736
	M-1.1	OC20++	0.313	0.632
		OMat24	0.204	0.450
		OMat24 \rightarrow MPTrj + sAlex	0.215	0.483

^a No strict neighbor enforcement.

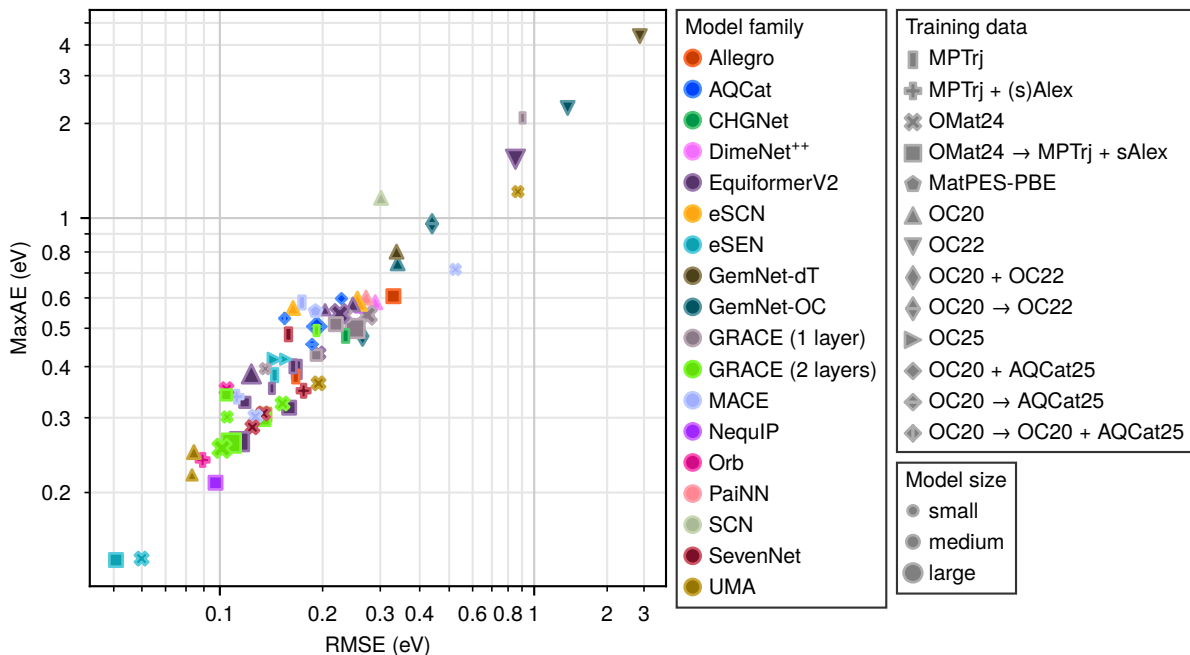


Figure S14: Prediction performance of the MLIPs for the reaction energy of the $\text{CO}_2 + \text{H} \rightleftharpoons \text{HCOO}$ reaction step on metal-supported metal oxide nanoclusters.

Table S15: Prediction performance of the MLIPs for the reaction energy of the $\text{CO}_2 + \text{H} \rightleftharpoons \text{HCOO}$ reaction step on metal-supported metal oxide nanoclusters.

Model family	Variant	Training data set	RMSE (eV)	MaxAE (eV)
Allegro	L-0.1	MPTTrj	0.166	0.378
		OMat24 → MPTTrj + sAlex	0.330	0.606
AQCat	31M	OC20 → AQCat25	0.186	0.455
	153M	OC20 → AQCat25	0.192	0.505
	31M inFiLM	OC20 → OC20 + AQCat25	0.154	0.530
	31M in+midFiLM	OC20 + AQCat25	0.228	0.598
CHGNet		MPTTrj	0.235	0.478
DimeNet ⁺⁺		OC20 (All)	0.289	0.584
EquiformerV2	31M	MPTTrj	0.505	0.988
		OMat24	0.276	0.546
		OMat24 → MPTTrj + sAlex	0.118	0.327
		OC20 (All+MD)	0.204	0.558
	31M DeNS	MPTTrj	0.142	0.353
	83M	OC20 (2M)	0.247	0.577
	86M	OMat24	0.194	0.431
		OMat24 → MPTTrj + sAlex	0.159	0.317
	86M DeNS	MPTTrj	0.163	0.401
	121M ($\lambda_E = 4, \lambda_F = 100$)	OC22	0.851	1.52
153M	OMat24	0.225	0.546	
	OMat24 → MPTTrj + sAlex	0.114	0.263	
	OC20 (All+MD)	0.123	0.384	
	MPTTrj	0.168	0.394	
eSCN	153M DeNS	MPTTrj	0.168	0.394
	$M = 2, 12$ layers	OC20 (All+MD)	0.163	0.565
	$M = 3, 20$ layers	OC20 (All+MD)	0.255	0.588
eSEN	30M	MPTTrj	0.144	0.381
		OMat24	0.0599	0.141
		OMat24 → MPTTrj + sAlex	0.0507	0.140
	small conserving	OC25	0.155	0.417
	medium direct	OC25	0.144	0.416

^a No strict neighbor enforcement.

Table S15: Prediction performance of the MLIPs for the reaction energy of the $\text{CO}_2 + \text{H} \rightleftharpoons \text{HCOO}$ reaction step on metal-supported metal oxide nanoclusters.

Model family	Variant	Training data set	RMSE (eV)	MaxAE (eV)
GemNet	dT	OC20 (All)	0.337	0.801
		OC22	2.86	4.36
	OC	OC20 (All)	0.340	0.744
		OC22	1.35	2.27
		OC20 + OC22	0.264	0.477
	GRACE	OC ^a	OC20 \rightarrow OC22	0.439
1 layer small		OC20 + OC22	0.264	0.477
		MPTrj	0.904	2.09
1 layer medium		OMat24	0.135	0.395
		OMat24 \rightarrow MPTrj + sAlex	0.191	0.427
1 layer large		OMat24	0.234	0.540
		OMat24 \rightarrow MPTrj + sAlex	0.219	0.512
2 layers small		OMat24	0.273	0.541
		OMat24 \rightarrow MPTrj + sAlex	0.251	0.499
		2 layers medium	MPTrj	0.192
	OMat24		0.105	0.301
	2 layers large	OMat24 \rightarrow MPTrj + sAlex	0.104	0.341
		OMat24	0.152	0.325
MACE	MP-0a small	OMat24 \rightarrow MPTrj + sAlex	0.134	0.298
	MP-0a medium	OMat24	0.101	0.254
	MP-0a large	OMat24 \rightarrow MPTrj + sAlex	0.108	0.261
	MP-0b3 medium	MPTrj	0.319	0.713
	MPA-0 medium	MPTrj	0.174	0.584
	OMAT-0 small	MPTrj	0.273	0.618
	OMAT-0 medium	MPTrj	0.180	0.481
	MatPES-PBE-0	MPTrj + sAlex	0.112	0.337
		OMat24	0.524	0.716
NequIP	L-0.1	OMat24	0.127	0.302
		MatPES-PBE	0.190	0.554
Orb	conservative, 20 neighbors	MPTrj	0.257	0.573
		OMat24 \rightarrow MPTrj + sAlex	0.0972	0.211
	conservative, ∞ neighbors	MPTrj + Alex	0.0892	0.238
		OMat24 (only AIMD)	0.105	0.352
	direct, 20 neighbors	MPTrj + Alex	0.103	0.256
		OMat24 (only AIMD)	0.136	0.314
	direct, ∞ neighbors	MPTrj + Alex	0.144	0.384
		OMat24 (only AIMD)	0.189	0.406
PaiNN	SCN	MPTrj + Alex	0.0931	0.240
		OMat24 (only AIMD)	0.138	0.421
SevenNet	0	OC20 (All)	0.271	0.601
		OC20 (All+MD)	0.302	1.15
	13i5	MPTrj	0.174	0.462
		OMat24	0.124	0.285
	MF	MPTrj	0.158	0.482
OMat24		0.133	0.307	
UMA	S-1.1	MPTrj + sAlex	0.176	0.349
		OC20++	0.0833	0.220
	M-1.1	OMat24	0.869	1.20
		OMat24 \rightarrow MPTrj + sAlex	0.0843	0.249
		OMat24	0.194	0.364
		OMat24 \rightarrow MPTrj + sAlex	0.135	0.305

^a No strict neighbor enforcement.

S3 Poor prediction of magnetic elements

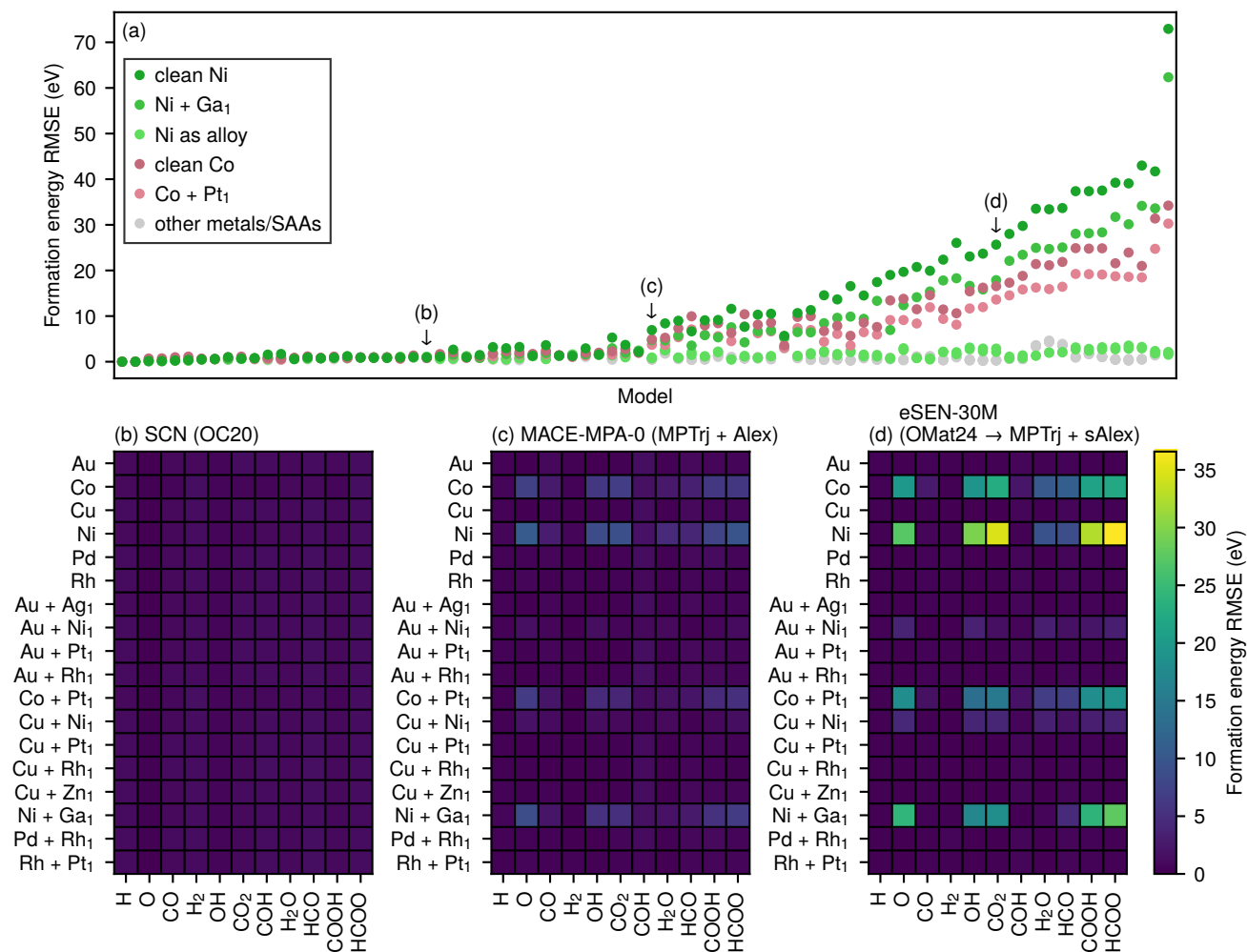


Figure S15: Formation energy predictions for reaction intermediates on metals and SAAs. (a) RMSE values for each combination of model and surface composition. Each column corresponds to one of the evaluated models, sorted by formation energy RMSE across the entire data set. Ni- and Co-containing surfaces have been indicated with green and red, respectively. (b–d) RMSE values for each combination of surface composition and adsorbate for three representative models: (b) a model trained on OC20, showing low errors for all combinations; (c) a model trained on MPTrj + Alex, showing somewhat increased errors for specific combinations; (d) a model trained on OAM, showing significant errors for specific combinations. Note that the errors in this figure have not been corrected as outlined in Section 2.4 as the high-error outliers would skew the results for the low-error combinations.

References

1. Cheula, R., Tran, T. A. M. Q. & Andersen, M. Unraveling the Effect of Dopants in Zirconia-Based Catalysts for CO₂ Hydrogenation to Methanol. *ACS Catalysis* **14**, 13126–13135. ISSN: 2155-5435. <http://dx.doi.org/10.1021/acscatal.4c03206> (2024).
2. Cheula, R. & Andersen, M. Transition States Energies from Machine Learning: An Application to Reverse Water–Gas Shift on Single-Atom Alloys. *ACS Catalysis* **15**, 11377–11388. ISSN: 2155-5435. <http://dx.doi.org/10.1021/acscatal.5c02818> (2025).
3. Reichenbach, T., Walter, M., Moseler, M., Hammer, B. & Bruix, A. Effects of Gas-Phase Conditions and Particle Size on the Properties of Cu(111)-Supported Zn_yO_x Particles Revealed by Global Optimization and Ab Initio Thermodynamics. *The Journal of Physical Chemistry C* **123**, 30903–30916. ISSN: 1932-7455. <http://dx.doi.org/10.1021/acs.jpcc.9b07715> (2019).
4. Kempen, L. H. E. & Andersen, M. Inverse catalysts: tuning the composition and structure of oxide clusters through the metal support. *npj Computational Materials* **11**, 8. ISSN: 2057-3960. <http://dx.doi.org/10.1038/s41524-024-01507-z> (2025).
5. Nielsen, M. J., Kempen, L. H. E., de Neergaard Ravn, J., Cheula, R. & Andersen, M. Interpretable machine learned predictions of adsorption energies at the metal–oxide interface. *The Journal of Chemical Physics* **163**, 044708. ISSN: 1089-7690. <http://dx.doi.org/10.1063/5.0282674> (2025).